Phospholipase iPLA$_2$β Averts Ferroptosis by Eliminating Death Signal, 15HpETE-PE: Relevance to Parkinson's Disease

Wan-Yang Sun[1,2,3], Vladimir A. Tyurin[1], Karolina Mikulska-Ruminska[4,5],Indira H. Shrivastava[1,5], Bing Liu[5], Yu-Jia Zhai[2,3], Ming-Hai Pan[2,3], Hai-Biao Gong[2,3], Dan-Hua Lu[2,3], Jie Sun[2,3], Wen-Jun Duan[2,3], Sergey Korolev[6], Andrey Y. Abramov[7], Plamena R. Angelova[7,15], Ian Miller[6], Ofer Beharier[10], Gao-Wei Mao[1], Haider Dar[1], Alexandr A. Kapralov[1], Teresa G. Hastings[8], J. Timothy Greenamyre[8], Charleen T. Chu[9], Yoel Sadovsky[10], Ivet Bahar[5], Hülya Bayır[1,11], Yulia Y. Tyurina[1]**, Rong-Rong He[2,3]**,Valerian E. Kagan[1,12,13,14,15]**

[1]Department of Environmental and Occupational Health and Center for Free Radical and Antioxidant Health, University of Pittsburgh, Pittsburgh, Pennsylvania 15260, United States

[2]Guangdong Engineering Research Center of Chinese Medicine & Disease Susceptibility, [3]International Cooperative Laboratory of Traditional Chinese Medicine Modernization and Innovative Drug Development of Chinese Ministry of Education (MoE), College of Pharmacy, Jinan University, Guangzhou, Guangdong 510632, China

[4]Institute of Physics, Faculty of Physics Astronomy and Informatics, Nicolaus Copernicus University in Toruń, Grudziadzka 5, 87-100 Toruń, Poland.

[5]Department of Computational and Systems Biology, School of Medicine, University of Pittsburgh, Pennsylvania 15260, United States

[6]Edward A. Doisy Department of Biochemistry and Molecular Biology, Saint Louis University School of Medicine, St. Louis, Missouri 63104, United States

[7]UCL Queen Square Institute of Neurology, Department of Clinical and Movement Neurosciences, University College London, Queen Square, London WC1N 3BG, United Kingdom

[8]Department of Neurology, [9]Department of Pathology, [10]Magee Womens Research Institute and Department of OBGYN, University of Pittsburgh, Pittsburgh, Pennsylvania 15213, United States

[11]Department of Critical Care Medicine, Safar Center for Resuscitation Research, Children's Neuroscience Institute, Children's Hospital of Pittsburgh, University of Pittsburgh, Pittsburgh, Pennsylvania 15260, United States

[12]Department of Radiation Oncology, [13]Department of Chemistry, and [14]Department of Pharmacology and Chemical Biology, University of Pittsburgh, Pittsburgh, Pennsylvania 15260, USA,

[15]Institute of Regenerative Medicine, IM Sechenov Moscow State Medical University, Moscow 119048, Russia.

** - corresponding authors: kagan@pitt.edu; rongronghe@jnu.edu.cn; yyt1@pitt.edu

ABSTRACT

Ferroptosis is a cell death program triggered by metabolic discoordination of iron, thiols and lipids, leading to selective accumulation of 15-hydroperoxy-arachidonoyl-PE (15-HpETE-PE) generated by complexes formed between 15-lipoxygenase (15-LOX) and a scaffold protein, PEBP1. As Ca^{2+}-independent phospholipase PLA_2 ($iPLA_2\beta$), a product of the *PNPLA9* gene, can preferentially hydrolyze peroxidized phospholipids, we hypothesized that $iPLA_2\beta$ guards from the ferroptotic 15-HpETE-PE death signal. Here we demonstrate that by hydrolyzing 15-HpETE-PE, cytosolic $iPLA_2\beta$ averts ferroptosis whereas genetic or pharmacological inactivation of the enzyme sensitizes cells to ferroptosis. As several neurodegenerative diseases are related to mutations in the *PNPLA9* gene, we examined fibroblasts from a patient with a Parkinson's disease (PD)-associated mutation fPD^{R747W} and found selective loss of 15-HpETE-PE hydrolyzing activity, 15-HpETE-PE accumulation and elevated sensitivity to ferroptosis. CRISPR-CAS9-engineered $PNPLA9^{R748W/R748W}$ mice exhibited progressive parkinsonian motor deficits along with 15-HpETE-PE accumulation. Elevated 15-HpETE-PE levels were also detected in midbrain of rotenone-infused parkinsonian rats. Thus, $iPLA_2\beta$ is a new ferroptosis regulator and its mutations may be implicated in PD pathogenesis.

INTRODUCTION

Fidelity and quality control of biological systems depend on either re-programming or elimination of unnecessary or harmful cells and/or their organelles via several types of cell death programs[1, 2]. Ferroptosis is a newly discovered type of regulated cell death[3] triggered by discoordination of three major metabolic pillars – iron, lipids and thiols - and culminating in lipid peroxidation[3]. The term "ferroptosis" reflects two specific roles of iron in: i) the production of membrane (phospho)lipid (PL) hydroperoxides and ii) "splitting" the weak hydroperoxy O-O bond in the hydrophobic milieu of membranes[4] to yield oxidatively-truncated electrophilic products, considered as the proximate executioners of ferroptotic death[5]. A seleno-peroxidase, glutathione peroxidase 4 (GPX4), reduces membrane PL hydroperoxides to alcohols[6], thus "neutralizing" the high-risk O-O-containing intermediates[7-9].

Hydroperoxy-arachidonoyl-(C20:4, eicosatetraenoyl, ETE or AA)- and adrenoyl-(C22:4, docosa-tetraenoyl, DTE)-phosphatidylethanolamines (PE) (HpETE-PE and HpDTE-PE) have been identified as characteristic pro-ferroptotic signals [10,11]. Accordingly, enzymatic esterification of these two fatty acid residues into PE by ACSL4 and re-acylation of lyso-PE (LPE) by LPCAT3 are important ferroptosis regulators[13,14]. High selectivity and specificity of ETE-PE and DTE-PE oxidation at their 15th and 17th carbons, respectively, is a feature of ferroptotic lipid peroxidation[11], suggesting the involvement of enzymatic catalysis[12]. Indeed, 15-lipoxygenase (15-LOX) complexed with a scaffold-protein, PE-binding protein 1 (PEBP1), has been identified as a generator of pro-ferroptotic 15-HpETE-PE and 17-HpDTE-PE[13]. One can assume that a phospholipase A_2 capable of hydrolyzing *sn*-2-oxygenated polyunsaturated fatty acid (PUFA)-PE residues would eliminate the ferroptotic signal whereas genetic or chemical ablation of this activity would be pro-ferroptotic. Therefore, we focused our attention on Ca^{2+}-independent iPLA$_2\beta$ (PNPLA9 from *PLA2G6* family) which can hydrolyze oxidized phospholipids[14], yet its catalytic competence towards ferroptotic signals has not been hitherto tested.

Ferroptosis has been implicated in a number of acute conditions and chronic diseases, including Parkinson's disease (PD)[3, 15]. Death of dopaminergic neurons in the *substantia nigra pars compacta* is one of the hallmarks of PD[16]. Enhanced oxidative stress and lipid peroxidation caused by mishandling of iron and dopamine oxidation are important causative factors[17], along with dysregulation of autophagy[18] which otherwise regulates ferroptosis by degrading iron storage proteins[19]. Based on the striking similarity of the PD pathogenesis and triggers of ferroptosis, it has been suggested that ferroptosis may be involved in PD pathogenesis[16, 20, 21] through yet to be

discovered mechanisms. *PNPLA9* mutations have been associated with a series of iPLA$_2\beta$-associated neurodegenerative diseases (PLAN)[22]. Based on the age of onset and progressive clinical features, several PLAN subtypes have been identified: infantile neuroaxonal dystrophy (INAD), atypical neuroaxonal dystrophy (ANAD) and a Parkinsonian syndrome with adult onset dystonia and autosomal recessive early-onset Parkinsonism[23-25]. Thus, we have put forward and tested the hypothesis that deficiency in iPLA$_2\beta$ caused by genetic or pharmacological perturbations preserves the death signal, 15-HpETE-PE, hence propagates ferroptosis. Here we demonstrate that genetic abatement of iPLA$_2\beta$ in SH-SY5Y neuronal cells, H109 fibroblasts, and BeWo trophoblasts, or a naturally occurring mutation in the *PNPLA9* gene encoding for iPLA$_2\beta$ (*R747W*) in fibroblasts from a dystonic PD patient (fPD^{R747W} cells) result in: i) lowered hydrolytic activity towards 15-HpETE-PE, ii) elevated intracellular contents of 15-HpETE-PE, and iii) enhanced sensitivity to ferroptosis relative to WT controls. We further document that CRISPR-engineered *PNPLA9*$^{R748W/R748W}$ mice exhibit progressive parkinsonian motor deficits along with 15-HpETE-PE accumulation. We detected decreased iPLA$_2\beta$ activity and elevated 15-HpETE-PE levels in the midbrain of rotenone-infused parkinsonian rats. These experimental data along with computational/mathematical modeling permitted us to decipher and predict the impact of impairments of iPLA$_2\beta$ and its *R747W* mutant on ferroptotic death relevant to PD pathogenesis.

RESULTS

15-HpETE-PE is a preferred substrate of iPLA$_2\beta$. To assess iPLA$_2\beta$ hydrolytic activity (Fig. 1a,b), we biosynthesized 15-HpETE-PE and purified it to ~99% homogeneity (as evidenced by LC-MS analysis (Supplementary Fig. 1a). We also expressed, isolated and purified recombinant iPLA$_2\beta$[26] (Supplementary Fig. 1b) and tested its activity by LC-MS of the products: ETE or 15-HpETE, and LPE (Fig. 1c,d). While both substrates were readily hydrolyzed by the enzyme, the activity towards 15-HpETE-PE was markedly higher (3.1-fold for LPE and 7.7-fold for fatty acid) than towards non-oxidized PE (Fig. 1a,b, *insets*). We next performed computational modeling of enzyme's interactions with membrane phospholipid substrates. Molecular dynamics (MD) simulations of a neuronal membrane containing 15-HpETE-PE, ETE-PE and various PLs, (Supplementary Fig 2 and Methods) showed the ability of 15-HpETE-PEs to migrate within the lipid bilayer and expose their peroxidized acyl chains, originally embedded in the membrane, to the surface (Fig 2a and Supplementary Movie 1), driven by the tendency of the peroxidized group to escape the hydrophobic environment. This behavior is similar to the migration of peroxidized triglycerides to

the surface of lipid droplets [27]. The peroxy-group could explain the observed higher propensity of membrane-bound iPLA$_2\beta$ to preferentially interact with 15-HpETE-PE.

We further examined the interactions of the catalytically active iPLA$_2\beta$ dimer surrounded by ankyrin (ANK) segments (Fig.2b) with membrane-embedded 15-HpETE-PEs (Fig 2c,d). iPLA$_2\beta$ C651 was found to closely interact with the membrane, consistent with an earlier study[26], thus bringing the catalytic dyad [S465 and D598] into proximity of the bilayer surface, and enabling frequent encounters with 15-HpETE-PE (Fig. 2c,d). Quantitative analysis (Supplementary Fig. 3) showed that select residues (e.g. $K_{566}PLP_{568}$ and H517 in monomer A and R656-P657, W661, T650, K665 and F668 in monomer B) had the strongest interactions with 15-HpETE-PE.

R747W mutation reduces iPLA$_2\beta$ catalytic activity towards 15-HpETE-PE. A number of mutations in the catalytic domain (CAT) of the *PNPLA9* gene have been documented[26] and associated with several neuropathies and PD[22]. We tested the activity of one of them (*R747W*, or R693W in the short variant) and found that the mutant protein displayed a slightly lower activity towards non-oxidized ETE-PE and a markedly greater loss of activity towards 15-HpETE-PE (Fig. 1a,b). We next assessed the endogenous phospholipase activity in control and fPD^{R747W} cells using two different protocols to directly measure the hydrolytic potency of iPLA$_2\beta$ towards non-oxygenated substrates and 15-HpETE-PE (Fig. 3a) [28]. To distinguish between general PLA$_2$ activity and specific iPLA$_2\beta$ activity, we employed an inhibitor, (*S*)-bromoenol lactone ((*S*)-BEL), a chiral-specific suicidal substrate that discriminates iPLA$_2\beta$ from all other phospholipases**Error! Reference source not found.**29 (Supplementary Fig. 1c). General PLA$_2$ activity was slightly (1.3-fold) but significantly lower in fPD^{R747W} cells than in control cells (Fig. 3a *upper* panel). Importantly, the activity towards exogenously added 15-HpETE-PE was sharply lower (>5-fold) in fPD^{R747W} cells *vs* control cells (Fig. 3a, *lower* panel). Western blotting (Fig. 3b) showed no differences in iPLA$_2\beta$ content between control and fPD^{R747W} cells. Thus, *R747W* mutation specifically suppressed catalytic competence towards 15-HpETE-PE but not towards conventional PL substrates.

To explore the molecular basis of the lowered catalytic potency of *PNPLA9* mutant *R747W* towards 15-HpETE-PE, we repeated our simulations with the mutant dimer. The simulations showed that *R747W* mutation affected the interfacial packing between the two CAT domains of the dimer resulting in two effects: i) the catalytic site became less accessible, and ii) the association of the mutant with the membrane weakened (Fig. 2e,f). This supports the experimentally observed higher hydrolytic activityof the *R747W* mutant toward 15-HpETE-PE.

Sensitivity of fPD^{R747W} and iPLA$_2\beta$–deficient cells to ferroptosis. Next, we utilized redox phospholipidomics and determined the hydrolytic activity (Fig. 3c-e) and the content of oxidation products in WT H109 (fibroblasts from healthy patient) and fPD^{R747W} cells after triggering ferroptosis by a GPX4 inhibitor, RSL3 (Fig. 3d). fPD^{R747W} cells exhibited significantly higher levels of pro-ferroptotic 15-HpETE-PE both basally and after RSL3 induced ferroptosis: 15-HpETE-PE level was 2.4-fold higher in fPD^{R747W} cells than in WT cells (Fig. 3d).

We asked if the human PD-associated *R747W* mutation in *PNPLA9* increases the sensitivity of fPD^{R747W} cells to pro-ferroptotic stimulation. Thus we examined the time-course and concentration-dependence of cell death, triggered by RSL3 (Fig. 3f) and revealed a higher sensitivity to ferroptosis of fPD^{R747W}cells, both in terms of the lower RSL3 concentration required for the ferroptotic response and its earlier onset in the fPD^{R747W}cells. The specificity of RSL3-induced ferroptotic death was confirmed by negative responses to inhibitors of alternative death programs – apoptosis (z-VAD-fmk) and necroptosis (necrostatin-1s) (Fig. 3g), whereas four inhibitors of ferroptosis (Fer-1, DFO, Vitamin E (vit E), Baicalein) inhibited RSL3-induced cell death.

To explore whether iPLA$_2\beta$ anti-ferroptotic potential is realized in other cell types, we compared the sensitivity to ferroptosis in WT and several *PNPLA9* KD cells: H109 fibroblasts, SH-SY5Y neuronal cells and BeWo trophoblasts. These experiments demonstrated a markedly enhanced sensitivity of iPLA$_2\beta$–deficient cells to RSL3 induced ferroptosis *vs* WT controls (Fig. 3h and Supplementary Fig. 4a,b). Moreover, iPLA$_2\beta$–deficient cells exhibited higher levels of pro-ferroptotic PE biomarkers detected by LC-MS (Supplementary Fig. 4c).

Homozygous PNPLA9^{R747W} leads to a Parkinsonian phenotype in mice. Assuming that human *PNPLA9^{R747W}* mutation and the resultant deficiency of hydrolyzing activity towards pro-ferroptotic PE-derived signals lead to enhanced death of dopaminergic neurons in the *substantia nigra* accompanied by PD-linked symptoms, we employed by CRISPR/Cas genome editing, and created a mouse with a R748W point mutation at the mouse *PNPLA9* locus, corresponding to *R747W* of human *PNPLA9* (Fig. 4a and Supplementary Fig. 5,6). In the homozygous *PNPLA9*$^{R748W/R748W}$ mice, we observed motor impairments (Fig. 4b-d and Supplementary Fig. 7) documented using the pole test (Fig. 4b and Supplementary Movie 2) and rotarod test (Fig. 4c and Supplementary Movie 3) which started at age 3-4 months. Quantitative catwalk test indicated that *PNPLA9*$^{R748W/R748W}$ mice had reduced average walking speed, increased walking speed variation, and disrupted walking

cycle, when compared with WT and *PNPLA9*$^{WT/R748W}$ mice (Fig. 4d). Motor impairments were not detected in heterozygous *PNPLA9*$^{WT/R748W}$ mice, confirming the human data that only homozygous mutants develop behavioral deficiencies related to PD pathogenesis [30], and consistent with its role in causing autosomal recessive PD.

In homozygous *PNPLA9*$^{R748W/R748W}$ mutant mice, the midbrain levels of tyrosine hydroxylase (TH), a marker for dopaminergic neurons, were significantly decreased (Fig. 4e), indicating a more than 40% reduction of dopaminergic neurons. Consistently, dopamine (DA) - the product of TH - and its primary metabolites 3,4-dihydroxyphenylacetaldehyde (DOPAL) and 3-methoxytyramine (3-MT) in the striatum of mutant mice were also significantly decreased (Fig. 4f). We also observed elevated levels of a chartacteristic peroxidation product, 4-hydroxynonenal, 4-HNE (Fig. 4g), and lower contents of intracellular antioxidant glutathione, GSH (Fig. 4h) in the mutant mouse midbrain. Monomeric *α*-synuclein and *α*-synuclein aggregates did not accumulate in the mutant mice (Supplementary Fig. 8a,b).

Oxygenated PE in the midbrain of Homozygous PNPLA9^{R748W} mice. Comparative redox phospholipidomics analysis of midbrain samples revealed elevated levels of 15-HpETE-PE in *PNPLA9*$^{R748W/R748W}$ *vs.* WT mice (Fig. 4i), suggesting possible activation of ferroptosis in *PNPLA9* mutants. Assessment of the specific hydrolytic competency towards 15-HpETE-PE showed that the activity was sharply decreased (more than 75%) in the brain homogenates of *PNPLA9* mutant *vs* WT mice (Fig. 4j and Supplementary Fig. 8c). Western blotting showed no differences in the iPLA$_2$β protein contents between the two groups of mice (Fig. 4k).

Pro-ferroptotic oxygenated PE in midbrains of pharmacological PD rodent model. Using another PD model, rotenone infused rats (Fig. 5a), the redox lipidomics measurements revealed significantly elevated levels of pro-ferroptotic 15-HpETE-PE and 17-HpDTE-PE in midbrain tissue on days 10-14 after rotenone infusion(Fig. 5b-d), when the characteristic manifestations of PD-related syndrome are clearly detectable[31]. Direct assessments of the specific enzymatic activity towards 15-HpETE-PE revealed significantly lower rates of hydrolysis in rotenone-treated brain homogenates *vs* non-treated controls (Fig. 5e and Supplementary Fig. 9a).

Furthermore Western blotting of iPLA$_2$β revealed significantly decreased expression levels of the protein in the midbrain of 8-month-old SNCA-A53T mutant mice *vs* WT mice (Supplementary Fig. 9b). Of note, the SNCA-A53T mutation is associated with autosomal dominant PD and elicits a PD

disease-relevant phenotype in rodents[32]. It has been reported that A53T αSyn can indirectly – via suppression of mitogen-activated protein kinase (MAPK) signaling – negatively regulate the expression of *PNPLA9*[33].

Mathematical modeling of iPLA$_2$β in ferroptosis. To explore the role of iPLA$_2$β in regulatory ferroptosis network, we built a mathematical model of the metabolic reactions that regulate 15-HpETE-PE dynamics in cells (Fig. 6a-d and Supplementary Table 1). We simulated ferroptotic cell death by varying the iPLA$_2$β activity towards 15-HpETE-PE under different expression levels of GPX4 (Fig. 6e). Decreased iPLA$_2$β hydrolytic activity increased the sensitivity of H109 cells to ferroptosis triggers. When GPX4 was sufficiently expressed, perturbing iPLA$_2$β activity did not significantly influence cell death level, suggesting that iPLA$_2$β plays a complementary role to GPX4 in protecting cells against ferroptotic death. *In silico* testing the occurrence of ferroptotic death in response to different expression levels of GPX4, 15LOX, and iPLA$_2$β (Fig. 6f) showed that the efficacy of iPLA$_2$β in fPD^{R747W} cells in controlling ferroptosis was comparable to that of GPX4 and 15LOX. All three proteins acted as death/survival 'switches' even though their effects were opposite - pro-ferroptotic (15LOX) or anti-ferroptotic (GPX4 and iPLA$_2$β). However, in WT H109 cells, iPLA$_2$β acted as a 'rheostat' to fine-tune the ferroptotic response.

DISCUSSION

In spite of a relatively short history of research on ferroptosis, strong necro-inflammatory consequences of this death program and its possible pathogenic role in major acute and chronic degenerative diseases stimulated studies of its regulation. Identification of enzymatic mechanisms affecting the lipid arm of the ferroptotic network, such as ACSL4, LPCAT3[11], along with 15-HpETE-PE generation by 15LOX complexes with PEBP1[13] was followed by the discoveries of new regulatory cascades including FSP1[7, 8] and iNOS[9]. Thus, the key regulatory role of GPX4 in ferroptosis may be complemented or substituted by other important enzymatic mechanisms in a context-dependent manner. Here we demonstrate that iPLA$_2$β can act as an anti-ferroptotic guardian via elimination of the pro-ferroptotic signal, 15-HpETE-PE.

A conformational change consistent with the whisker model[34] proposed for peroxidized PLs allows for the exposure of the peroxidized acyl chain of 15-HpETE-PE to the membrane surface, thus enabling interfacial interaction with membrane-bound catalytic domains of the dimeric iPLA$_2$β. This alternative 15-HpETE-PE neutralizing mechanism may act in coordination with the reductive GPX4-

dependent pathway or independently of it, serving as an additional check-point for preventing unnecessary or excessive ferroptotic death. The role of this pathway may be particularly important when the thiol-driven defenses become insufficient. Consequently, failure or deficiency in iPLA$_2$β – caused by genetic factors or chemical/pharmacological poisoning - may be associated with increased sensitivity to ferroptotic death. Our demonstration of iPLA$_2$β insufficiency and resultant accumulation of 15-HpETE-PE in PD-associated models represents a new mechanism of PD pathogenesis and suggest that protectors against iPLA$_2$β inactivation may become useful for PD therapeutics.

Metabolic features of dopaminergic neurons with their high abundance of iron required for dopamine biosynthesis and high levels of redox-active intermediates of dopamine oxidation create pro-oxidant microenvironments[16]. Among the most common manifestations of this are GSH deficiency[35], suppressed activity of GPX4[36], and elevated levels of lipid peroxidation products[37] - all typical characteristics of cells primed to ferroptotic death[3]. Not surprisingly, possible engagement of ferroptotic death in PD pathogenesis has been widely discussed, yet specific mechanisms for triggering ferroptosis in PD dopaminergic neurons remained enigmatic[16]. The present study demonstrates that a typical PD-associated mutation in iPLA$_2$β results in a specific loss of catalytic activity towards one of the peroxidized PLs, the ferroptotic 15-HpETE-PE, in several cell culture and *in vivo* models. Interestingly, earlier work found no changes in the catalytic activity of iPLA$_2$β mutants associated with idiopathic PD[38]. However these assessments did not examine oxygenated phospholipids, particularly 15-HpETE-PE, as substraters of the hydrolyitic activity.

PNPLA9 mutations have been lnked to pathogenesis of several neurodegenerative diseases[22], including PD. To comparatively evaluate the effect of the *R747W* mutation on the iPLA$_2$β function and the pathogenicity potential vs. all possible mutations we performed *in silico* saturation mutagenesis analysis using a machine learning tool Rhapsody[39,39] (Supplementary Fig. 11). This analysis confirmed *a* highly deleterious nature and high pathogenicity score of the *R747W*. Mathematical modeling of HpETE-PE regulating reactions further endorsed our experimental data supporting the important anti-ferroptotic function of iPLA$_2$β and the role of *R747W* mutation in PD pathogenesis.

Our work demonstrates that, in addition to direct effects on iPLA$_2$β activity/expression, indirect regulatory factors altering iPLA$_2$β levels in critical cells/tissues may affect the ferroptotic signaling

via 15HpETE-PE. We found that iPLA$_2\beta$ expression was significantly reduced in a genetic model of rodent PD overexpressing the mutant A53T αSyn. Both WT and A53T αSyn suppressed MAPK signaling that regulates *PNPLA9* expression[33]. This could be attributed to the direct interaction of αSyn with MAPKs such as ERK2 and its substrate ELK1, a transcription factor that binds the promoter of *PNPLA9*[40, 41]. We demonstrated that the decreased expression of iPLA$_2\beta$ leads to a dampened pro-ferroptotic arachidonoyl-PE metabolism. Interestingly, a recent study in *Drosophila* showed that the loss of iPLA$_2\beta$ leads to the shortening of PL acyl chains, facilitating αSyn aggregation[42]. Thus, a vicious cycle involving αSyn overexpression and iPLA$_2\beta$ underexpression may be warranted.

Taken together, our experimental results and the *in silico* studies strongly suggest that ineffective control/destruction of pro-ferroptotic signals as a consequence of PD-related direct (*PNPLA9)*, or indirect mutations leading to the reduced enzymatic hydrolytic activity of iPLA$_2\beta$ following pesticide or other environmental exposure, may contribute to PD pathogenesis.

METHODS

Materials. 1-Octadecanoyl-2-(5*Z*,8*Z*,11*Z*,14*Z*-eicosatetraenoyl)-*sn*-glycero-3-phosphatidylethanol-amine (ETE-PE and 1-octadecanoyl-*sn*-glycero-3-phosphatidylethanolamine (LPE) were purchased from Avanti Polar Lipids. 5*Z*,8*Z*,11*Z*,14*Z*-Eicosatetraenoic acid (ETE) and 15(*S*)-hydroperoxy-5*Z*,8*Z*,11*Z*,13*E*-eicosatetraenoic acid (15-HpETE) were purchased from Cayman Chemical. Unless otherwise stated, all other reagents were HPLC grade and purchased from Fisher Scientific.

Animal models. The experiments were approved by the Institutional Animal Care and Use Committee at the University of Pittsburgh (rat rotenone model) and the Laboratory Animal Ethics Committee at Jinan University (A53T overexpression mouse model and *PNPLA9*^{R748W} mouse model). Animal care and handling were in accord with National Institutes of Health guidelines.

Rat rotenone model: Rats were randomized in each study, and in all cases the surgeon and researches evaluating the outcomes were blinded to the treatment group. Adult (7-9 months old, Charles River) male Lewis rats were subjected to a rotenone-induced model of PD as previously described[43]. Briefly, rats were injected intraperitoneally with vehicle or 3.0 mg/kg/day of rotenone (Sigma-Aldrich) either for one injection, for five daily injections, or treated to parkinsonian endpoint. Animals treated with rotenone to Parkinsonian endpoint (10-14 days) were sacrificed when animals displayed behavioral features including bradykinesia, postural instability/gait disturbances, and

rigidity. Rat brains were first removed from the skull and rinsed in cold 1× phosphate-buffered saline to remove any surface blood. The brains were placed on a cold Petri dish and cut in half into the right and left hemisphere. Using a blade and forceps precise micro-dissection of the ventral midbrain was performed and the tissue was flash frozen in liquid nitrogen and stored at 80 °C.

A53T overexpression mouse model: Hualpha-Syn (A53T) transgenic C57BL/6J mice were purchased from The Jackson Laboratory (Stock No: 006823) and bred in our laboratory. Animals were sacrificed at eight-months of age.

PNPLA9^{R748W} mouse model: CRISPR/Cas-mediated genome engineering was used to create a C57BL/6N mouse model with point mutation (R748W) at mouse *PNPLA9* locus. Briefly, the gRNAs to mouse *PNPLA9* gene, the donor oligo containing R748W (CGG to TGG) mutation, and Cas9 were co-injected into fertilized mouse eggs to generate targeted knockin offspring. Two silent mutations (GCC to GCG at A749) and (GGC to GGG at G755) was introduced to prevent the binding and re-cutting of the sequence by gRNA after homology-directed repair. F0 founder animals were identified by PCR followed by sequence analysis, which were bred to wild-type mice to test germline transmission and F1 animal generation. The homozygous mutant mice were further generated by inter-cross heterozygous mutant mice. The gRNA target sequence are as follows: gRNA1 (F1, matching reverse strand of gene): GATGCCGACCATCTCGCACCAGG; gRNA2 (R1, matching forward strand of gene): CTGTGGATCGGGCCCGGGCCTGG. Animals were sacrificed at seven-month-old.

Cell lines. H109 and fPD^{R747W} cells, the human primary skin fibroblasts obtained from a healthy and a *R747W PNPLA9* dystonia Parkinsonism patients[28], were cultured in Dulbecco's modified Eagle's medium (DMEM) medium (ATCC) supplemented with 10% fetal bovine serum (FBS) (Sigma-Aldrich) and 50 U/ml penicillin-streptomycin (Thermo Fisher Scientific). SH-SY5Y cells (ATCC, CRL-2266) purchased from ATCC were cultured in 1:1 mixture of Eagle's Minimum Essential Medium (EMEM) and F-12K Medium (1:1) supplemented with 10% FBS and antibiotics. BeWo human trophoblast cells (ATCC, CCL-98) purchased from ATCC were cultured in F-12K medium supplemented with 10% FBS and antibiotics. Cells were grown in incubators with controlled temperature of 37 °C, 5% CO_2, and 95% humidity. RNAi plasmid were encoded by shRNAs against *PNPLA9.*

Lentivirus vectors encoding shPNPLA9 (GCTGACGCCCTAGTGAATTTC) were used to knockdown iPLA$_2\beta$ in H109 and SH-SY5Y cells according to the manufacturer's instructions (Integrated Biotech Solutions Co., Ltd.). The pGMLV-SC5 lentiviral vector system was applied to deliver shPNPLA9 into DH5α cells according to manufacturer's instructions. The obtained plasmids

were extracted and sequenced. Besides, bulk plasmid was prepared for transfection. Briefly, the plasmid was diluted with serum-free OMEM (Gibco) and incubated with Lipofectamine 3000 (Thermo Fisher). Cells were transfected with the mixture for 6 h, and then the medium was replaced and the cells were cultured for 40 h. Transfection efficiency was optimized using a range of plasmid and Lipofectamine 3000 concentrations.

PNPLA9 knockout in BeWo cells. BeWo cell line that stably express the doxycycline-inducible Cas9 plasmid (Addgene plasmid #50661) was used for knocking out *PNPLA9.* Guide RNAs were designed using the CRISPR design tool (MIT), and expressed from pLKO5.sgRNA.EFS.tRFP657 (Addgene plasmid #57824) lentiviral system, initially in HEK293 cells, with virus used to infect BeWo cells (Guererro and Y Sadovsky, in submission.)

Ferroptosis assay. H109 and fPD^{R747W} cells were treated with RSL3 (25 nM) for 14 h in the absence or in the presence of ferrostatin-1 (Fer-1, 0.4 μM). For evaluation the specificity of RSL3 induced ferroptotic cell death, cells were incubated with RSL3 (25 nM) in the presence of z-VAD-fmk (Zvad, 50 μM) or necrostatin-1s (Nec-1s, 20 μM), Fer-1 (0.4 μM), deferoxamine (DFO, 10 μM), vitamin E (Ve, 10 μM), or baicalein (2 μM). SH-SY5Y and iPLA$_2$β knockdown cells were incubated with RSL3 (2 μM) for 18 h in the absence or in the presence of Fer-1 (0.4 μM). BeWo WT and *PNPLA9* KO cells were incubated with RSL3 (100 nM) for 12 h in the absence or in the presence of Fer-1 (0.4 μM). Cell death was detected by LDH release using the CytoTox-ONE™ Cyto-toxicity Detection Kit (Promega).

Protein cloning, expression, and purification (iPLA$_2$β). Short variant CHO iPLA$_2$β was cloned and expressed as described previously [26]. The short variant lacks a 54 amino acid (396-450) insert between ankyrin repeats and catalytic domain. The numbering is adjusted accordingly, such that *R747W* in Human Long iPLA$_2$β is R693W in the CHO construct. CHO and human proteins have 90.4% sequence identity and identical length of both variants. Briefly, the pFastBac vector containing the *PNPLA9* gene cloned from CHO cells with a C-terminal 6XHisTag was used for protein expression. Cloning of the CHO R693W mutant was achieved via Quikchange mutagenesis protocol using Phusion HS High Fidelity polymerase (Thermo Fisher). Single amino acid substitution was confirmed by complete sequencing of the gene (Source BioScience). The CHO iPLA$_2$β protein was expressed in Sf9 cells (Invitrogen) using the Bac-to-Bac system. Bacmid DNA was transfected into Sf9 cells with Trans-IT transfection reagent (Mirus Bio). After 4 days, the media were collected as the p0 viral stock. This stock was amplified by adding 1 ml of p0 to 100 ml of 2 × 10^6 cells/ml for 96 h, creating the p1 viral stock. 25ml of the amplified p1 was used to infect 500 ml

shaker flasks of 2 × 10^6 cells/ml for 72 h. The cells were centrifuged at 1000 rpm, and the pellet was washed with cold phosphate-buffered saline (PBS) before being suspended in purification buffer (25 mM HEPES pH 7.5, 20% glycerol, 0.5 M NaCl, 1 mM TCEP) containing 50 µg/ml each of leupeptin and aprotinin. The cell suspension was frozen in liquid nitrogen and lysed by thawing and sonication at 50% power, 50% pulse cycle four times for 2 min each. The lysate was cleared by ultracentrifugation at 100,000 × g for 1 h. Urea of 0.5 M and TCEP of 1 mM were added to the supernatant and mixed with 5 ml of TALON cobalt resin (Clontech) to bind for 1 h at 4 °C. The resin was centrifuged at 800 × g for 4 min to remove the flow-through fraction in batch mode. The resin containing the bound protein was then applied to an empty column, washed sequentially with purification buffer containing 10 mM imidazole (100 ml), 40 mM imidazole (2 x 5 ml), and eluted with purification buffer containing 250 mM imidazole (2 x 5 ml). iPLA$_2$β and its mutant (R693W) were >95% pure as determined by sodium dodecyl sulfate-polyacrylamide gel electrophoresis (SDS-PAGE) and Coomassie staining (Supplementary Fig. 1). Activity of purified proteins was confirmed as described previously [26] using fluorescent phospholipase activity assay with 1-hexadecanoyl-2-(1-pyrenedecanoyl)-*sn*-glycero-3-phosphatidylcholine (Pyrene-PC, Thermo Fisher #H361).

Assessment of iPLA$_2$β activity. Model system: iPLA$_2$β activity was assessed by formation of hydrolysis products of ETE-PE (LPE-18:0/0:0 and ETE) or 15-HpETE-PE (LPE-18:0/0:0 and 15-HpETE) in the absence and in the presence of (*S*)-BEL, a chiral-specific non-reversible inhibitor of iPLA$_2$β. Recombinant WT or *R747W* mutant enzyme (0.5 µg) was added to 100 µM ETE-PE or 15-HpETE-PE in 50 mM PBS (pH=7.4) containing DTPA (100 µM). Samples were incubated for 15 min at 37 °C. The reaction was stopped by addition of chloroform:methanol (2:1, v/v). Hydrolysis products were extracted and resolved by LC/MS.

Cells and tissues: Cells (1 x 10^6) were harvested by trypsinization, washed with PBS, re-suspended in 20 mM HEPES and 1% of 1× protease inhibitor (pH 7.4), sonicated on ice, and centrifuged at 12,000 g for 15 min. Tissues homogenates were centrifuged at 12000 g for 15 min as well. Supernatants were used to assess activity of iPLA$_2$β. Cells or tissues supernatants (150 µg protein) were added to 50 mM HEPES (pH=7.4) containing 7 µM ETE-PE or 15-HpETE-PE, 100 mM NaCl, and 5 mM EGTA and incubated for 30 min at 37 ^{o}C. For (*S*)-BEL-treated group, supernatants were pre-incubated with (*S*)-BEL (10 µM) for 10 min at 37 ^{o}C. Reaction was stopped by addition of chloroform:methanol 2:1, v/v. Hydrolysis products were extracted and analyzed by LC/MS. The activity of iPLA$_2$β was expressed in mU/min per mg of protein.

Western blotting analysis. Cells and tissues were resuspended in lysis buffer (25 mM Tris-HCl, pH 7.5, 150 mM NaCl, and 1% SDS) (Thermo Fisher) containing protease-phosphatase cocktail inhibitor mixture (Thermo Fisher) on ice. Samples were sonicated to break down DNA and total protein amount was estimated by BCA protein assay kit (Thermo Fisher). Samples were diluted in 2X-6X Laemmli buffer before loading in 8–16% Tris-glycine gradient gels (Life Technologies) and proteins transferred to nitrocellulose or polyvinylidene difluoride (PVDF) membranes (Bio-Rad) and blocked with milk (5%) in PBST (0.1% Tween). Proteins expression was detected using anti-iPLA$_2\beta$ (polyclonal, PA5-27945, Thermo Fisher), anti-tyrosine hydroxylase (ab112, abcam), anti-*α*-synuclein (SC-7011-R, Santa Crz), anti-4-HNE (ab46545, abcam), anti-GAPDH (FD0063, Fude Biotech), and anti-β-actin (mouse monoclonal, A3854, clone AC-15, Sigma-Aldrich) antibodies (1% BSA in PBST) overnight at RT, washed 3 times, and incubated with horseradish peroxidase (HRP)-conjugated secondary antibody-goat anti-rabbit IgG (A0545, Sigma-Aldrich, FDR07, Fude Biotech) and goat anti-mouse IgG (FDM07, Fude Biotech) (1 hr) in blocking solution before developing with SuperSignal West Pico Chemiluminescent Substrate (Thermo Fisher). The bands were visualized using X-ray film, imaged using Amersham Imager 600 (GE Health Care, Life Sciences) and quantified using ImageJ software (NIH). The integrated density value was obtained by integrating the entire pixel values in the area of one band after correction for background. All blots were re-probed with actin antibody for loading corrections.

LC-MS/MS analysis of ETE-PE and 15-HpETE-PE hydrolysis products. LPE-18:0/0:0, was analyzed by LC/MS using a Q-Exactive Hybrid Quadrupole-Orbitrap Mass Spectrometer (Thermo Fisher). Analytes were separated on a hydrophilic interaction liquid chromatography (HILIC) column (Macmod HILIC Column, 90Å, 2.7 µm, 0.5 mm X 150 mm (Reading)) at a flow rate of 35 µL/min on a Dionex Ultimate 3000 RSLCnano System. The column was maintained at 35 °C. A gradient solvent system that consisted of solvent A (isopropanol:hexane:water (285:215:5, v/v/v)) and solvent B (isopropanol:hexane:water (285:215:40, v/v/v)), each containing 10 mM ammonium formate, was used as follows: 0-23 min linear gradient of 10 to 30% B, 23-45 min linear gradient of 30% to 100% B, 45-52 min isocratic of 100% B, and 52-60 min re-equilibration of 10% B. Analysis was performed in negative ion mode at a resolution of 140,000 full width at half maximum (FWHM) for the full MS scan in a data-dependent mode. The scan range for MS analysis was 400-1800 *m/z* with a maximum injection time of 128 ms using 1 microscan. An isolation window of 1.0 Da was set for the MS1 and MS2 scans. Capillary spray voltage was set at 3.5 kV, and capillary temperature was 320 °C. The S-lens RF level was set to 60. Sheath gas flow rate was set at 10 AU. Quantitation of the lipids was performed using Xcalibur 4.2 Quan Browser (Thermo Fisher).

ETE and 15-HpETE were analyzed by LC/MS using a Dionex Ultimate 3000 HPLC system coupled on-line to a Q-Exactive Hybrid Quadrupole-Orbitrap mass spectrometer (Thermo Fisher) using a C18 column (Acclaim PepMap RSLC, 100 Å, 5 µm, 150 mm × 0.3 mm, Thermo Fisher). The analysis was performed using gradient solvents (A and B) containing 5 mM ammonium acetate at a flow rate of 12 µL/min. All solvents were LC-MS-grade. The column was eluted using a linear gradient from 30% solvent B to 95% solvent B over 70 min, held at 95% B from 70 to 80 min followed by a return to initial conditions by 83 min and re-equilibration for an additional 7 min. Spectra were acquired in negative ion mode at a resolution of 140,000 for the full MS scan in a data-dependent mode. The scan range for MS analysis was *m/z* 150-600 with a maximum injection time of 100 ms using 1 microscan. An isolation window of 1.0 Da was set for the MS and MS^2 scans. Capillary spray voltage was set at 2.6 kV, and capillary temperature was 250 °C. The S-lens RF level was set to 60. Analytical data were acquired and analyzed using Xcalibur 4.2 Quan Browser (Thermo Fisher).

LC-MS/MS analysis of PLs in cells and tissues. Lipids were extracted using the Folch procedure, and phosphorus was determined by a micro-method as described previously[3]. PLs were analyzed by LC/MS using a Dionex Ultimate 3000 HPLC system coupled on-line to a Q-Exactive Hybrid Quadrupole-Orbitrap Mass Spectrometer (Thermo Fisher) using a normal phase column (Luna 3 µm Silica (2) 100 Å, 150 × 2.0 mm, (Phenomenex)). The column was maintained at 35 °C. The analysis was performed using gradient solvents (A and B) containing 10 mM ammonium formate at a flow rate of 0.2 ml/min. Solvent A contained isopropanol/hexane/water (285:215:5, v/v/v), and solvent B contained isopropanol/ hexane/water (285:215:40, v/v/v). All solvents were LC/MS-grade. The column was eluted for 0-23 min with a linear gradient from 10% to 32% B; 23-32 min with a linear gradient of 32%–65% B; 32-35 min with a linear gradient of 65%–100% B; 35-62 min held at 100% B; 62-64 min with a linear gradient from 100% to 10% B; followed by an equilibration from 64-80 min at 10% B. Analysis was performed in negative ion mode at a resolution of 140,000 for the full MS scan in a data-dependent mode. The scan range for MS analysis was *m/z* 400-1800 with a maximum injection time of 128 ms using 1 microscan. An isolation window of 1.0 Da was set for the MS1 and MS2 scans. Capillary spray voltage was set at 3.5 kV, and capillary temperature was 320 °C. The S-lens RF level was set to 60. Analysis of raw LC/MS data was performed using software package Compound Discoverer™ 2.0 (Thermo Fisher) with an in-house generated analysis workflow and oxidized PL database. Briefly, peaks with S/N ratio of more than 3 were identified and searched against oxidized PL database. Lipids were further filtered by retention time

and confirmed by a fragmentation mass spectrum. Deuterated PLs (Avanti Polar Lipids) were used as internal standards. Values for *m/z* were matched within 5 ppm to identify the lipid species.

Identification of 15-HpETE-PE. 15-HpETE-PE was identified by MS/MS analysis using an Orbitrap™ Fusion™ Lumos™ mass spectrometer (Thermo Fisher). The instrument was operated with an electrospray ionization probe in negative polarity mode. Ion source conditions were set as follows: spray voltage = 4 kV, sheath gas = 20 (arbitrary unit), auxiliary gas = 4 (arbitrary unit), sweep gas = 0 (arbitrary unit), transfer tube temperature = 300 °C, RF-Lens level = 50%. Data were acquired in data-dependant-MS^2 targeted-MS^3 mode with a Cycle Time setting of 3 s. For MS scan events, the parameters were set as follow: Ion detection = Orbitrap, mass resolution = 120,000, scan range = *m/z* 400 - 1800, AGC target = 1e5. The most intense ion was selected for the data-dependent MS^2 scan. The dynamic exclusion was set to 9 s. The exclusion mass list for MS^2 was created from solvent blank injection data. For MS^2 scan event(s), the parameters were set as follows: quadrupole isolation = 1 Da, first Mass = *m/z* 87, activation type = HCD, collision energy = 24%, ion detection = Orbitrap, mass resolution = 15,000, max Injection time = 250 ms, AGC target = 2e4. Product ions from a targeted mass list were selected for MS3 scan. The target mass list for MS3 included 74 ions for a variety of potential oxidized fatty acyl products. For MS^3 scan event(s), the parameters were set as follows: isolation window = 2.0 Da, activation type = CID, collision energy = 35%, ion detection = ion Trap, ion trap scan rate = rapid, max injection time = 500 ms, AGC target = 5e4.

LC-MS/MS analysis of catecholamine neurotransmitters and GSH. Catecholamine neurotransmitters and GSH were determined by LC-MS/MS using a Triple Quad 4500 Mass Spectrometer (SCIEX) (Supplementary Table 3). Analytes were separated on a C18 column (Acquity HSS T3, 1.8 µm, 2.1 mm X 100 mm, Waters) at a flow rate of 0.4 mL/min on an Exion LC AD system. The column was maintained at 40 °C. A gradient solvent system that consisted of solvent A (water) and solvent B (acetonitrile), each containing 0.1% formic acid (v/v), was used as follows: 0-1.2 min isocratic of 2% B, 1.2-2.5 min linear gradient of 2 to 60% B, 2.5-4.5 min linear gradient of 60% to 95% B, 4.5-5.0 min isocratic of 95% B, and 5.0-6.5 min re-equilibration of 2% B. Analysis was performed in switched positive and negative ion modes using scheduled multiple reaction monitoring scan method. Capillary spray voltage was set at 5.5 and -4.5 kV, and ion source temperature was 600 °C. Nebulizer gas and heater gas was set to 55 psi, and curtain gas was set to 30 abr. Data acquisition and processing were carried out using Analyst 1.6.2 software (SCIEX).

Computational modeling of iPLA$_2$β dimer structure. iPLA$_2$β structure (752 residues) complexed with ankyrin fragments was constructed using the available structure (PDB code: 6aun[44]) and a combination of homology modeling and *ab initio* simulations. The missing fragments in the X-ray structure of iPLA$_2$β dimer (UniProt ID: A0A384E119), i.e. M1-A80, Y95-R115, L129-N145, R405-K408 and V652-A670, were reconstructed using Swiss Model[45] and I-tasser[46] servers.

Construction and equilibration of neuronal lipid bilayer. Neuronal membrane containing 15-HpETE-PE (4%), ETE-PE (SAPE, 22%) and various PLs (SAPI 4%, SOPC 15%, PSPC 25%, SOPE 5%, OLPS 10%, PAPC 5%, SDPE 10%), the composition of which has been deduced from lipidomics data, has been prepared using CHARMM-GUI[47] and in-house scripts. The membrane size was 50 x 50 x 50 Å. The same composition and spatial distribution have been replicated to construct larger membranes (100 x 100 Å^2 and 250 x 250 Å^2 surface area and 50 Å depth) to avoid end effects. Equilibration simulations were performed for 50 x 50 x 50 Å membrane using NAMD[48] software with CHARMM force field[49] and explicit water model (TIP3P)[50]. The simulated system contained over 51,000 atoms, including the lipid and water molecules, and KCl ions. Six preparatory simulations were conducted before the main run following CHARMM-GUI protocols[47]. Two main 100 ns MD simulations were performed where the additional polar oxygen atoms-containing acyl chains of ETE-PE reoriented and partially protruded from the membrane surface into the aqueous solution. Force field parameters for 15-HpETE-PE were created using SwissParam[51]. The structural model of 15-HpETE-PE was built and minimized using Maestro[52].

Molecular Dynamics (MD) Simulations of iPLA$_2$β dynamics, bound to the lipid bilayer. Equilibrated membrane with protruding acyl chain of 15-HpETE-PE was replicated to perform protein-membrane simulations. The dimeric protein orientation (CAT domain (M416-P752) and full structure of iPLA$_2$β (M1-P752)) in the membrane was predicted by PPM server[53]. The systems contained over 320,000 atoms (100 x 100 x 115 Å box, CAT domains) and 750,000 atoms (200 x 200 x 125 Å, iPLA$_2$β dimer). The following protocol was adopted using NAMD[48] package: 0.2 ns of water equilibration, 10,000 steps of minimization, 0.35 ns of heating from 0 to 300 K, and 0.15 ns equilibration of the whole system before initiating the production MD run. Eight trajectories (four for WT and R693W, each), with CAT domain dimer in close proximity to the membrane were generated, each 55 ns long with 2 fs timesteps. Four 20 ns trajectories with the full structure of iPLA$_2$β dimer were also computed. A cutoff of 12 Å was adopted for non-bonded interactions. Langevin dynamics and Langevin piston algorithm[54] were used to maintain the temperature at 300 K and the pressure at 1 atm. We used VMD[55] for visualization.

Elastic network model analysis. In order to identify the cooperative motions of iPLA$_2$β dimer, we performed a Gaussian Network Model (GNM) analysis, using *Prody*[56] with a cutoff distance of 7.3 Å and generated the covariance map that describes the coupled motions of different domains. The corresponding positive (*red*) and negative (*blue*) regions indicate the structural regions subject to concerted correlated and anticorrelated (coupled but opposite direction) conformational changes, respectively. The correlation values were normalized to vary from -1 (full anticorrelation; *dark blue*) to 1 (full correlation; *dark red*). Allosteric properties of the dimer were deduced from perturbation response scanning (PRS) analysis[57, 58]. PRS provides maps in which the ij^{th} element describes the effect of perturbing residue *i* on the dynamics of residue *j*. The average perturbation caused over all residues is called effectiveness and indicates the ability of residue *i* to instigate cooperative changes in dynamics. In turn, the average effect of all residues on the j^{th} represents the sensitivity of residue *j* to the perturbations. The strongest effectors and sensors can be interpreted as effective senders and receivers of allosteric signals[59, 60]. PRS was performed using *ProDy*[56] together with in-house codes.

***in silico* saturation mutagenesis analysis**. The tool Rhapsody[39] developed for predicting the functional consequences of single amino acid variants (SAVs) was used for automated scanning of all iPLA$_2$β residue substitutions. The method uses a Random Forest-based classifier trained using an integrated dataset of 20,854 missense mutations functionally characterized to date. For each protein, eight structural, sequence-based, and dynamics-based features are calculated using ProDy[56, 61] and PolyPhen-2[62], inputting iPLA$_2$β structure (PDB id: 6AUN). The reported Rhapsody, PolyPhen-2, and EVmutation[63] scores represent the probability of causing a deleterious effect on function[64].

Mathematical modeling. We constructed a mathematical model for the metabolic pathways regulating ferroptosis. The reaction network is shown in Fig. 6a and the acronyms are in Supplementary Table 1. ASCL4 catalyzes the association between AA and CoA to form AA-CoA, which is in turn converted into ETE-PE by LPCAT3. 15LOX catalyzes the generation of 15-HpETE-PE from ETE-PE, which triggers ferroptosis. The death signal 15-HpETE-PE is reduced into HETE-PE by GPX4 or cleaved into 15-HpETE and LPE-18:0/0:0 by iPLA$_2$β. The time evolution of the system is described by 13 ODEs (Supplementary Table 1). Reaction rates were modeled using Michaelis-Menten and mass action kinetics as in our previous model[3]. We used the LSODA algorithm to solve the ODE system, an integrated 15-HpETE-PE concentration over time to predict

cell death level. Unknown kinetic parameters were estimated using training experimental data (Fig. 6b and c) by our statistical model checking methods[65] and further validated by independent test data (Fig. 6d). The resulting parameters are summarized in Supplementary Table 1.

Behavioral studies. Pole test: Pole test was used to evaluate the mouse movement disorder. The instrument consists of an iron stand (height, 60 cm; diameter, 0.8 cm) with a small ball wrapped with gauze at the top. In the test, the mice were placed on the top of a small ball and the time required for the mouse to climb down the pole was recorded. The test was measured 3 times per mouse and the maximum time was recorded.

Rotarod test: Rotarod performance was used to assess mouse motor balance and coordination. Mice were trained for 3 days prior to treatment to adapt to the rotarod apparatus (Zhenghua Co., Anhui, China). After training, on the 7th day, mice were placed in the separate runway on the rod and at a constant speed of 25 rpm every day at the same time. Each mouse was tested three times. The latency to fall was recorded.

Catwalk test: CatWalk Gait Analysis is a system for rodent gait analysis. The apparatus consists of a long glass walking plate, a fluorescent light beamed into the glass plate and a high-speed video camera under the glass plate. In a dark environment, the light was reflected downward and a camera mounted under the glass recorded the footprint of mouse on the walkway[66]. Mice were trained to cross the glass walkway three days prior to the test. After last drug administration, the mouse performed unforced and uninterrupted moving at least three times. The data of mouse gait was qualitatively and quantitatively analyzed by the automated gait analysis system CatWalk (Noldus Information Technology, Wageningen, the Netherlands).

Statistical analysis.The results are presented as mean ± standard deviation (SD) with a minimum of three replicates unless otherwise specified. Statistical analyses were performed by either Student's *t*-test or one-way/two-way ANOVA for normally distributed data. When the overall ANOVA revealed a significant effect, the data were further analyzed with the Dunnett/Sidak post hoc test to determine specific group differences. The statistical significance of differences was set at $P<0.05$. Differences between the groups were analyzed by Prism 8.1 (GraphPad Software, Inc).

Data availability: Data generated during the study and included in this article are available from the corresponding authors upon request.

ACKNOWLEDGEMENTS: This work was supported by NIH (HL114453-06, U19AI068021, CA165065-06, NS076511, NS061817, P41GM103712, R21NS094854, PA30DA035778 and P01DK096990), Natural Science Foundation of China (81873209, 81622050, 81903821), 111 Project of Chinese MoE (B13038), the Local Innovative and Research Teams Project of Guangdong Pearl River Talents Program (2017BT01Y036), GDUPS (2019), and the March of Dimes Prematurity Research Center at the University of Pennsylvania.

AUTHOR CONTRIBUTIONS: VEK, RRH, HB, YYT and YS conceived the study. YJZ, OB, HD and OK performed experiments with cells. SK and IM cloned and purified the WT and mutant iPLA$_2$β protein. VEK, HB, CTC, TGH, RRH and WJD designed *in vivo* experiments; WYS, MHP, DHL and JS performed *in vivo* experiments. VEK, YS, YYT, HB, AYA, PRA and RRH designed *in vitro* experiments; WYS and VAT performed *in vitro* experiments. WYS, VAT and HBG performed MS measurements and analyzed data. WYS, YYT and VAT discussed and interpreted MS results. KM-R, IHS and BL performed computational modeling. IB supervised computational studies and interpreted the results. WYS, IB, YS, CC, HIS, BL and HB participated in writing the manuscript. YYT and VEK wrote the manuscript.

DECLARATION OF INTERESTS: The authors have declared that no conflict of interest exists.

FIGURE LEGENDS

Fig. 1. Effect of point mutation on iPLA$_2$β function. a) Formation of LPE-18:0/0:0 in reactions catalyzed by mutant *R747W* or WT iPLA$_2$β. Data are means±SD, *n*=3. *Insert*: Differences (Δ) in levels of LPE formed by WT and *R747W* iPLA$_2$β. ETE-PE (blue) and 15-HpETE-PE (red) were used as substrates. Data are means±SD, **P*<0.05, ***P*<0.01, *n*=3, two-way ANOVA (Sidak post-hoc test). **b**) Formation of ETE and 15-HpETE-PE in reactions catalyzed by mutant *R747W* or WT iPLA$_2$β. ETE-PE (blue) and 15-HpETE-PE (red) were used as substrates. Data are means±SD, *n*=3. *Insert*: Differences (Δ) in the levels of ETE and 15-HpETE formed by WT and *R747W* iPLA$_2$β. Data are means±SD, **P*<0.05, ****P*<0.001, *n*=3, two-way ANOVA (Sidak post-hoc test). **c**) Schema showing hydrolysis of 1-stearoyl-2-15-HpETE-PE by iPLA$_2$β. **d)** Detection and identification of 1-stearoyl-2-15-HpETE-PE hydrolysis products catalized by iPLA$_2$β: 15-HpETE (upper panels) and LPE-18:0/0:0 (lover panels). Base peak chromatograms of molecular ions with *m/z* 335.2224 and *m/z* 480.3096 corresponding to 15-HpETE and LPE-18:0/0:0, respectively (left panels). MS^2 fragmentation patterns of molecular ions with *m/z* 335.2224 and *m/z* 480.3096, corresponding to

15-HpETE and LPE-18:0/0:0, respectively. *Inserts*: respective structures and fragments formed during MS^2 analysis (right panels).

Fig. 2. Interaction of the iPLA$_2$β dimer with membrane embedded PLs. a) Snapshot from MD simulations of neuronal membrane showing reorientation and migration of HpETE-PE peroxidized acyl chain after 50ns simulation (see Supplementary Fig. 2 for details) **b**) Intact structural model for iPLA$_2$β dimer CAT domains with ANK repeats bound to lipid bilayer **c**) Simulation system (*side view*:*top* and *top view*:*bottom*) contained lipid bilayer and iPLA$_2$β. ANK fragments are anchored to membrane surface. Cys651 makes close contacts (< 5.0 Å) with 15-HpETE-PE molecules (in *cyan space-filling* representation, oxygens in *red*). Each monomer's catalytic dyads (S465 and D598) are shown in *red* **d**) iPLA2β monomers A (*red*) and B (*blue*) with catalytic dyad in *magenta* and *R747W* in *orange* (*left*). Two PLs closely interact with iPLA2β: 15-HpETE with K566-P567 on chain A and SDPE with R656-P657 on chain B. Note that iPLA2β residues are inserted into membrane and PLs protrude to allow tight (>3.5Å atom-atom) associations **e-f**) Comparison of structure and interactions of wt iPLA2β (**e**) and *R747W* mutant (**f**). Equilibrated structures are comparable (e-f panels 1). Major change occurs in an interfacial cavity that closes down in the mutant (encircled by *dashed white shapes* in panels *2)*, thus restricting access to catalytic site. A closeup view of this region is shown in panels *3*. An alternative conformation by mutant occurs resulting in weaker contacts with lipid membrane (e-f panels 4). Residue numbers refer to short-variant (PDB id: 6AUN[26]) except for *R747* (R693 in short variant) which refers to the gene *PNPLA9* numbering.

Fig. 3. iPLA$_2$β-deficient cells are sensitive to RSL3-induced ferroptosis. a) iPLA$_2$β activity in H109 and fPD^{R747W} cells. ETE-PE (*upper*) and 15-HpETE-PE (*lower*) were used as substrates. Data are means±SD, **P*<0.05, ****P*<0.001, *n*=3, unpaired two-tailed *t*-test. **b**) iPLA$_2$β protein expression in H109 and fPD^{R747W} cells. *Insert*: Representative western blot of iPLA$_2$β. Data are means±SD, ns, not significant, *n*=3. **c**) Typical mass spectra of PE from H109 and fPD^{R747W} cells **d**) Content of 15-HpETE-PE in RSL3 treated H109 and fPD^{R747W} cells. Data are means±SD, **P*<0.05, ****P*<0.001 *vs* WT, *n* = 3, two-way ANOVA (Sidak post-hoc test). **e**) LC-MS identification of 15-HpETE-PE in RSL3 treated fPD^{R747W} cells**.** Base peak chromatogram (*left*), MS^2 (*upper right*) and MS^3 (*lower right*) spectra of 1-steraoyl-2-15-HpETE-PE (*m/z* 798.5292). Insets: structural formula and fragments **f**) Time course of RSL3-induced ferroptosis (*upper*) and concentration-dependent effect of RSL3 (*lower*) in WT H109 and fPD^{R747W} cells. Data are means±SD, ***P*<0.01, ****P*<0.001 *vs* H109, *n*=3, two-way ANOVA (Dunnett post-hoc test). IC_{50} was 28.9nM and 22.0nM for H109 and fPD^{R747W}, respectively. **g**) Effect of inhibitors (Zvad: z-VAD-fmk 50μM, Nec-1s: necrostatin-1s 20μM, Fer-1:

ferrostatin-1 0.4μM, DFO: deferoxamine 10μM, vit E: vitamin E 10μM, baicalein 2μM) on RSL3-induced (25nM, 14 h) death in H109 (*upper*) and fPD^{R747W} (*lower*) cells. Data are means±SD, ***P<0.001 *vs* Control, $^{###}P$<0.001 *vs* RSL3, n=3, one-way ANOVA (Dunnett post-hoc test). **h)** RSL3-induced ferroptosis in WT and iPLA$_2$β KD H109 cells and WT. Data are means ± SD, ***P<0.001 *vs* WT, n = 3. Cell death was quantified by LDH release. unpaired two-tailed t-test.

Fig. 4. Homozygous *PNPLA9*^{R748W} leads to Parkinsonian phenotype and ferroptotic oxygenated PE accumulation in midbrain of mice. a) Schematic illustration of the genotyping strategy **b**) Time (sec) taken to climb down the pole, and **c**) time (sec) on the rotarod for WT and *PNPLA9* R748W mutant mice at 2-7 months of age. $^{###}P$<0.001 *vs* *PNPLA9*$^{WT/WT}$, ***P<0.001 *vs* *PNPLA9*$^{WT/R748W}$, n=6, two-way ANOVA (Sidak post-hoc test). **d**) Average walking speed (*left*), walking speed variation (*middle*), and cadence (*right*) of WT and *PNPLA9* R748W mutant mice at 7 months of age in the catwalk test. ***P<0.001, n=6, two-way ANOVA (Sidak post-hoc test). **e**) Tyrosine hydroxylase (TH) expression in midbrain of WT and *PNPLA9*$^{R748W/R748W}$ mice. Inset: Representative immunoblot. Data are means±SD, ***P<0.001, n=5, unpaired two-tailed t-test. **f**) Heat map of dopamine and its metabolites in striatum of WT and *PNPLA9*$^{R748W/R748W}$ mice, unpaired two-tailed t-test. **g**) Representative immunoblot (*left*) and quantitative analysis (*right*) of 4-HNE expression, and **h**) Glutathione (GSH) levels in midbrain of WT and *PNPLA9*$^{R748W/R748W}$ mice. Data are means±SD, **P<0.01, *P<0.05, n=5, unpaired two-tailed t-test. **i**) 15-HpETE-PE (known pro-ferroptotic signals) and **j**) iPLA$_2$β activity in midbrain of WT and *PNPLA9*$^{R748W/R748W}$ mice. 15-HpETE-PE was used as a substrate. **k**) Representative immunoblot (*top*) and quantitative analysis (*bottom*) of iPLA$_2$β protein expression; Data are means±SD, *P<0.05, **P<0.01, ns: not significant, n=5 for iPLA$_2$β protein expression studies and 6 for all others, unpaired two-tailed t-test.

Fig. 5. Accumulation of ferroptotic cell death signals in *substantia nigra* of rats exposed to rotenone. a) Schema of the study design. **b**) Typical mass spectrum of PE obtained from *substantia nigra* of rats on days 10-14 after exposure to rotenone. Inset: Mass spectrum of PE in the range of *m/z* from 798.40 to 798.58 (*left*) and in the range of *m/z* from 826.40 to 826.60 (*right*). **c**) Volcano plots of rotenone-induced changes in the levels of oxygenated PEs [log$_2$(fold change)] *vs* significance [-log$_{10}$(P-value)] by t-test in *substantia nigra* of rats exposed to vehicle or rotenone (ip, 3 mg/kg/day) at Parkinsonian endpoint (Day 10-14). Yellow, red, blue, and white circles represent PE plus 1, 2, 3, and 4 oxygens, respectively. n = 6. **d**) Quantitative assessments of 15-HpETE-PE and 17-HpDTE-PE (known pro-ferroptotic signals) in *substantia nigra* of vehicle and rotenone-treated rats. Data are means ± SD, **P<0.01, ***P<0.001, n = 5-9, two-way ANOVA (Sidak post-

hoc test). **e**) iPLA$_2$β activity in *substantia nigra* of vehicle and rotenone-treated rats. 15-HpETE-PE was used as a substrate. Data are means ± SD, ***P*<0.01, ****P*<0.001, *n* = 3-5, two-way ANOVA (Sidak post-hoc test).

Fig. 6. Mathematical modeling of ferroptotic pathways regulated by iPLA$_2$β. a) Schematic diagram of reaction network model. See Supplementary Table 1 for corresponding kinetic equations and parameters. **b**) Comparison of model predictions with experimental data on accumulation of ETE-PE and 15-HpETE-PE hydrolysis product LPE-(18:0/0:0). iPLA$_2$β-catalyzed hydrolysis of ETE-PE and 15-HpETE-PE was assumed to obey Michaelis-Menten kinetics. The rate constants for wild-type iPLA$_2$β and *R747W* mutant were estimated by fitting time course measurements of hydrolysis products. **c**) Comparison of model predictions with experimental data on 15-HpETE-PE and 15-HETE-PE levels in H109 and fPD^{R747W} cells in the presence of RSL3, and cell death in response to various RSL3 concentrations. Other kinetic parameters were adopted from a previous study[3]. Unknown parameters specific to H109 and fPD^{R747W} cells were estimated by fitting the measured ratios of 15-HpETE-PE/ETE-PE in response to 25 nM 14 h RSL3 treatment and ferroptotic death of H109 and fPD^{R747W} cells in response to different RSL3 doses. **d**) Comparison of model predictions with independent validation data on H109, H109 iPLA$_2$β KD and fPD^{R747W} cells death in response to RSL3+/-Fer-1. The model's predictive ability is further demonstrated by comparison with experimental data on the responses of WT H109, H109 iPLA$_2$β KD and fPD^{R747W} cells to perturbations by RSL3 and Fer-1. **e**) RSL3-induced ferroptotic death in response to different combinations of rate parameters of iPLA$_2$β activity towards 15-HpETE-PE and GPX4 expression levels. **f**) Cell death as a function of initial concentrations of iPLA$_2$β, GPX4 and 15LOX in H109 (*left*) and fPD^{R747W} (*right*) cells.

References

1. Galluzzi, L. *et al.* Molecular mechanisms of cell death: recommendations of the Nomenclature Committee on Cell Death 2018. *Cell Death Differ* **25**, 486-541 (2018).
2. Conrad, M., Angeli, J.P., Vandenabeele, P. & Stockwell, B.R. Regulated necrosis: disease relevance and therapeutic opportunities. *Nat Rev Drug Discov* **15**, 348-366 (2016).
3. Kagan, V.E. *et al.* Oxidized arachidonic and adrenic PEs navigate cells to ferroptosis. *Nat Chem Biol* **13**, 81-90 (2017).

4. Stoyanovsky, D.A. *et al.* Iron catalysis of lipid peroxidation in ferroptosis: Regulated enzymatic or random free radical reaction? *Free Radic Biol Med* **133**, 153-161 (2019).
5. Gugiu, B.G. *et al.* Identification of oxidatively truncated ethanolamine phospholipids in retina and their generation from polyunsaturated phosphatidylethanolamines. *Chem Res Toxicol* **19**, 262-271 (2006).
6. Ursini, F., Maiorino, M., Valente, M., Ferri, L. & Gregolin, C. Purification from pig liver of a protein which protects liposomes and biomembranes from peroxidative degradation and exhibits glutathione peroxidase activity on phosphatidylcholine hydroperoxides. *Biochim Biophys Acta* **710**, 197-211 (1982).
7. Bersuker, K. *et al.* The CoQ oxidoreductase FSP1 acts parallel to GPX4 to inhibit ferroptosis. *Nature* **575**, 688-692 (2019).
8. Doll, S. *et al.* FSP1 is a glutathione-independent ferroptosis suppressor. *Nature* **575**, 693-698 (2019).
9. Kapralov, A.A. *et al.* Redox lipid reprogramming commands susceptibility of macrophages and microglia to ferroptotic death. *Nat Chem Biol* **16**, 278-290 (2020).
10. Friedmann Angeli, J.P. *et al.* Inactivation of the ferroptosis regulator Gpx4 triggers acute renal failure in mice. *Nat Cell Biol* **16**, 1180-1191 (2014).
11. Doll, S. *et al.* ACSL4 dictates ferroptosis sensitivity by shaping cellular lipid composition. *Nat Chem Biol* **13**, 91-98 (2017).
12. Anthonymuthu, T.S. *et al.* Empowerment of 15-Lipoxygenase Catalytic Competence in Selective Oxidation of Membrane ETE-PE to Ferroptotic Death Signals, HpETE-PE. *J Am Chem Soc* **140**, 17835-17839 (2018).
13. Wenzel, S.E. *et al.* PEBP1 Wardens Ferroptosis by Enabling Lipoxygenase Generation of Lipid Death Signals. *Cell* **171**, 628-641 e626 (2017).
14. Liu, G.Y. *et al.* The phospholipase iPLA2gamma is a major mediator releasing oxidized aliphatic chains from cardiolipin, integrating mitochondrial bioenergetics and signaling. *J Biol Chem* **292**, 10672-10684 (2017).
15. Magtanong, L. & Dixon, S.J. Ferroptosis and Brain Injury. *Dev Neurosci*, 1-14 (2019).
16. Guiney, S.J., Adlard, P.A., Bush, A.I., Finkelstein, D.I. & Ayton, S. Ferroptosis and cell death mechanisms in Parkinson's disease. *Neurochem Int* **104**, 34-48 (2017).
17. Jenner, P., Dexter, D.T., Sian, J., Schapira, A.H. & Marsden, C.D. Oxidative stress as a cause of nigral cell death in Parkinson's disease and incidental Lewy body disease. The Royal Kings and Queens Parkinson's Disease Research Group. *Ann Neurol* **32 Suppl**, S82-87 (1992).
18. Chu, C.T. Mechanisms of selective autophagy and mitophagy: Implications for neurodegenerative diseases. *Neurobiol Dis* **122**, 23-34 (2019).
19. Gao, M. *et al.* Ferroptosis is an autophagic cell death process. *Cell Res* **26**, 1021-1032 (2016).
20. Do Van, B. *et al.* Ferroptosis, a newly characterized form of cell death in Parkinson's disease that is regulated by PKC. *Neurobiology of Disease* **94**, 169-178 (2016).

21. Artyukhova, M.A. *et al.* Interrogating Parkinson's disease associated redox targets: Potential application of CRISPR editing. *Free Radic Biol Med* (2019).
22. Guo, Y.P., Tang, B.S. & Guo, J.F. PLA2G6-Associated Neurodegeneration (PLAN): Review of Clinical Phenotypes and Genotypes. *Front Neurol* **9**, 1100 (2018).
23. Malaguti, M.C. *et al.* A novel homozygous PLA2G6 mutation causes dystonia-parkinsonism. *Parkinsonism Relat Disord* **21**, 337-339 (2015).
24. Gui, Y.X. *et al.* Four novel rare mutations of PLA2G6 in Chinese population with Parkinson's disease. *Parkinsonism Relat Disord* **19**, 21-26 (2013).
25. Kauther, K.M., Hoft, C., Rissling, I., Oertel, W.H. & Moller, J.C. The PLA2G6 gene in early-onset Parkinson's disease. *Mov Disord* **26**, 2415-2417 (2011).
26. Malley, K.R. *et al.* The structure of iPLA2beta reveals dimeric active sites and suggests mechanisms of regulation and localization. *Nat Commun* **9**, 765 (2018).
27. Mohammadyani, D. *et al.* Molecular speciation and dynamics of oxidized triacylglycerols in lipid droplets: Mass spectrometry and coarse-grained simulations. *Free Radic Biol Med* **76**, 53-60 (2014).
28. Kinghorn, K.J. *et al.* Loss of PLA2G6 leads to elevated mitochondrial lipid peroxidation and mitochondrial dysfunction. *Brain* **138**, 1801-1816 (2015).
29. Jenkins, C.M., Han, X., Mancuso, D.J. & Gross, R.W. Identification of calcium-independent phospholipase A2 (iPLA2) beta, and not iPLA2gamma, as the mediator of arginine vasopressin-induced arachidonic acid release in A-10 smooth muscle cells. Enantioselective mechanism-based discrimination of mammalian iPLA2s. *J Biol Chem* **277**, 32807-32814 (2002).
30. Paisan-Ruiz, C. *et al.* Characterization of PLA2G6 as a locus for dystonia-parkinsonism. *Ann Neurol* **65**, 19-23 (2009).
31. Panov, A. *et al.* Rotenone model of Parkinson disease: multiple brain mitochondria dysfunctions after short term systemic rotenone intoxication. *J Biol Chem* **280**, 42026-42035 (2005).
32. Zygogianni, O. *et al.* In Vivo Phenotyping of Familial Parkinson's Disease with Human Induced Pluripotent Stem Cells: A Proof-of-Concept Study. *Neurochem Res* **44**, 1475-1493 (2019).
33. Iwata, A., Maruyama, M., Kanazawa, I. & Nukina, N. alpha-Synuclein affects the MAPK pathway and accelerates cell death. *J Biol Chem* **276**, 45320-45329 (2001).
34. Greenberg, M.E. *et al.* The lipid whisker model of the structure of oxidized cell membranes. *J Biol Chem* **283**, 2385-2396 (2008).
35. Sian, J. *et al.* Alterations in glutathione levels in Parkinson's disease and other neurodegenerative disorders affecting basal ganglia. *Ann Neurol* **36**, 348-355 (1994).
36. Hauser, D.N., Dukes, A.A., Mortimer, A.D. & Hastings, T.G. Dopamine quinone modifies and decreases the abundance of the mitochondrial selenoprotein glutathione peroxidase 4. *Free Radic Biol Med* **65**, 419-427 (2013).
37. Dexter, D. *et al.* Lipid peroxidation as cause of nigral cell death in Parkinson's disease. *Lancet* **2**, 639-640 (1986).
38. Zhou, Q. *et al.* Impairment of PARK14-dependent Ca(2+) signalling is a novel determinant of Parkinson's disease. *Nat Commun* **7**, 10332 (2016).

39. Ponzoni, L. & Bahar, I. Structural dynamics is a determinant of the functional significance of missense variants. *Proc Natl Acad Sci U S A* **115**, 4164-4169 (2018).
40. Matys, V. *et al.* TRANSFAC and its module TRANSCompel: transcriptional gene regulation in eukaryotes. *Nucleic Acids Res* **34**, D108-110 (2006).
41. Consortium, E.P. The ENCODE (ENCyclopedia Of DNA Elements) Project. *Science* **306**, 636-640 (2004).
42. Mori, A. *et al.* Parkinson's disease-associated iPLA2-VIA/PLA2G6 regulates neuronal functions and alpha-synuclein stability through membrane remodeling. *Proc Natl Acad Sci U S A* **116**, 20689-20699 (2019).
43. Greenamyre, J.T., Cannon, J.R., Drolet, R. & Mastroberardino, P.G. Lessons from the rotenone model of Parkinson's disease. *Trends Pharmacol Sci* **31**, 141-142; author reply 142-143 (2010).
44. Malley, K.R. *et al.* The structure of iPLA 2 β reveals dimeric active sites and suggests mechanisms of regulation and localization. *Nature Commun.* **9**, 1-11 (2018).
45. Schwede, T., Kopp, J., Guex, N. & Peitsch, M. SWISS-MODEL: an automated protein homology-modeling server. *Nucl. Aci. Res.* **31**, 3381-3385 (2003).
46. Roy, A., Kucukural, A. & Zhang, Y. I-TASSER: a unified platform for automated protein structure and function prediction. *Nature protocols* **5**, 725-738 (2010).
47. Jo, S., Lim, J.B., Klauda, J.B. & Im, W. CHARMM-GUI Membrane Builder for mixed bilayers and its application to yeast membranes. *Biophysical Journal* **97**, 50-58 (2009).
48. Phillips, J. *et al.* Scalable molecular dynamics with NAMD. *J. Comput. Chem.* **26**, 1781-1802 (2005).
49. MacKerell Jr, A. *et al.* All-Atom Empirical Potential for Molecular Modeling and Dynamics Studies of Proteins. *J. Phys. Chem. B* **102**, 3586-3616 (1998).
50. Miyamoto, S. & Kollman, P.A. SETTLE: an analytical version of the SHAKE and RATTLE algorithm for rigid water models. *J. Comp. Chem.* **13**, 952-962 (1992).
51. Zoete, V., Cuendet, M.A., Grosdidier, A. & Michielin, O. SwissParam: a fast force field generation tool for small organic molecules. *J. Comp. Chem.* **32**, 2359-2368 (2011).
52. Steffan, R. & Kuhlen, T. MAESTRO - a tool for interactive assembly simulation in virtual environments. In: Fröhlich B., Deisinger J., Bullinger HJ. (eds) Immersive Projection Technology and Virtual Environments 2001. Eurographics. Springer, Vienna. (2001).
53. Lomize, M.A., Pogozheva, I.D., Joo, H., Mosberg, H.I. & Lomize, A.L. OPM database and PPM web server: resources for positioning of proteins in membranes. *Nucl. Aci. Res.* **40**, D370-D376 (2011).
54. Feller, S.E., Zhang, Y. & Pastor, R.W. Constant pressure molecular dynamics simulation: The Langevin piston method. *J. Chem. Phys.* **103**, 4613 (1995).
55. Humphrey, W., Dalke, A. & Schulten, K. VMD: visual molecular dynamics. *J. Mol. Graph.* **14**, 33-38 (1996).
56. Bakan, A. *et al.* Evol and ProDy for bridging protein sequence evolution and structural dynamics. *Bioinformatics* **30**, 2681-2683 (2014).

57. Atilgan, C., Gerek, Z., Ozkan, S. & Atilgan, A. Manipulation of conformational change in proteins by single-residue perturbations. *Biophys. J.* **99**, 933-943 (2010).
58. Atilgan, C. & Atilgan, A.R. Perturbation-response scanning reveals ligand entry-exit mechanisms of ferric binding protein. *PLoS Comput. Biol.* **5**, e1000544 (2009).
59. Verkhivker, G.M. Dynamics-based community analysis and perturbation response scanning of allosteric interaction networks in the TRAP1 chaperone structures dissect molecular linkage between conformational asymmetry and sequential ATP hydrolysis. *Bioch. Biophys. Acta* **1866**, 899-912 (2018).
60. Mikulska-Ruminska, K. *et al.* Characterization of Differential Dynamics, Specificity, and Allostery of Lipoxygenase Family Members. *J. Chem. Inform. Model.* **59**, 2496-2508 (2019).
61. Bakan, A., Meireles, L.M. & Bahar, I. ProDy: protein dynamics inferred from theory and experiments. *Bioinformatics* **27**, 1575-1577 (2011).
62. Adzhubei, I.A. *et al.* A method and server for predicting damaging missense mutations. *Nat Methods* **7**, 248-249 (2010).
63. Hopf, T.A. *et al.* Mutation effects predicted from sequence co-variation. *Nat Biotechnol* **35**, 128-135 (2017).
64. Ponzoni, L., Penaherrera, D.A., Oltvai, Z.N. & Bahar, I. Rhapsody: Predicting the pathogenicity of human missense variants. *Bioinformatics* (2020).
65. Liu, B., Gyori, B. & Thiagarajan, P. Statistical model checking based analysis of biological betworks. *Automated Reasoning for Systems Biology and Medicine*, 63-92 (2019).
66. Wang, X.H. *et al.* Quantitative assessment of gait and neurochemical correlation in a classical murine model of Parkinson's disease. *BMC Neurosci* **13**, 142 (2012).

Figures

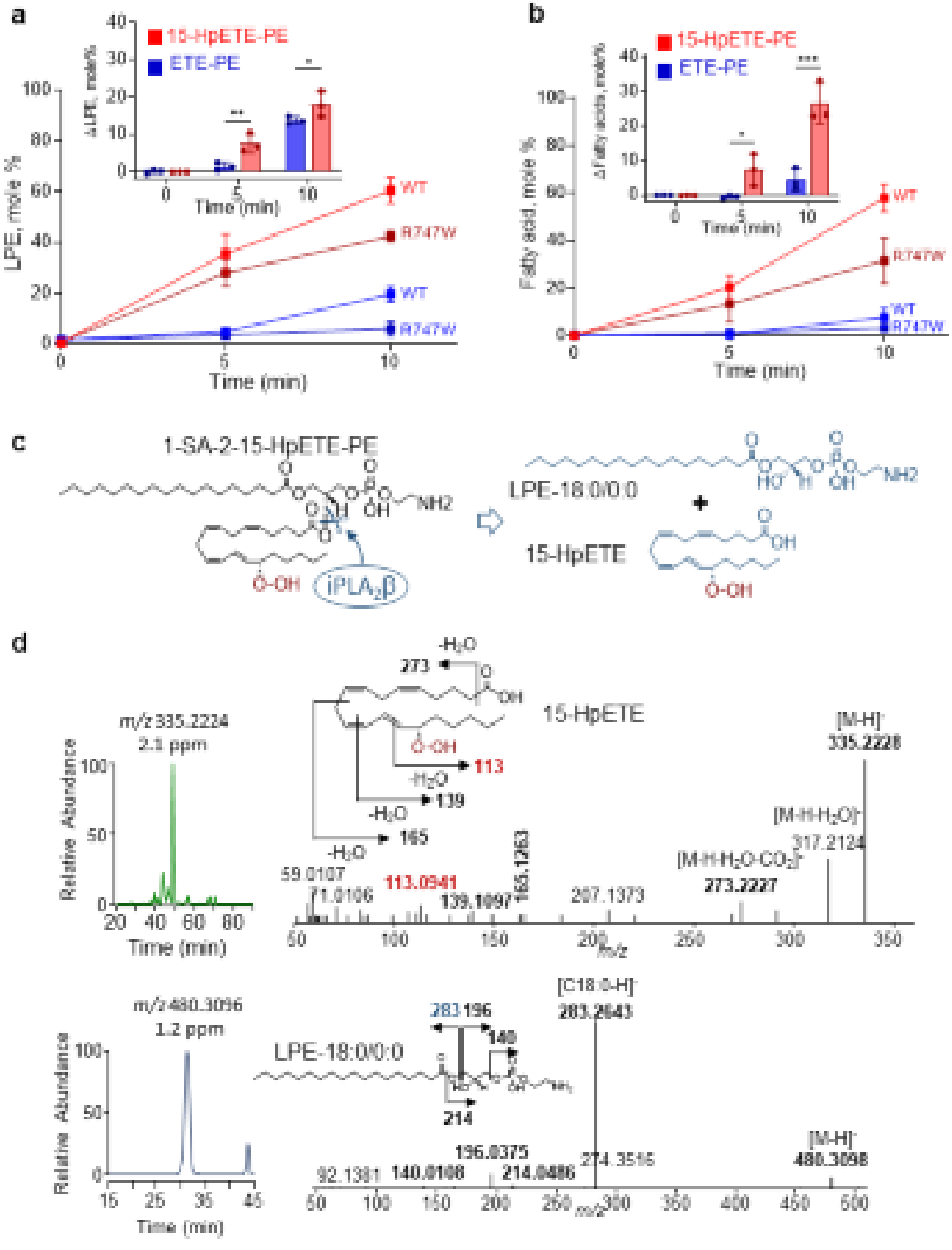

Figure 1

Figure 2

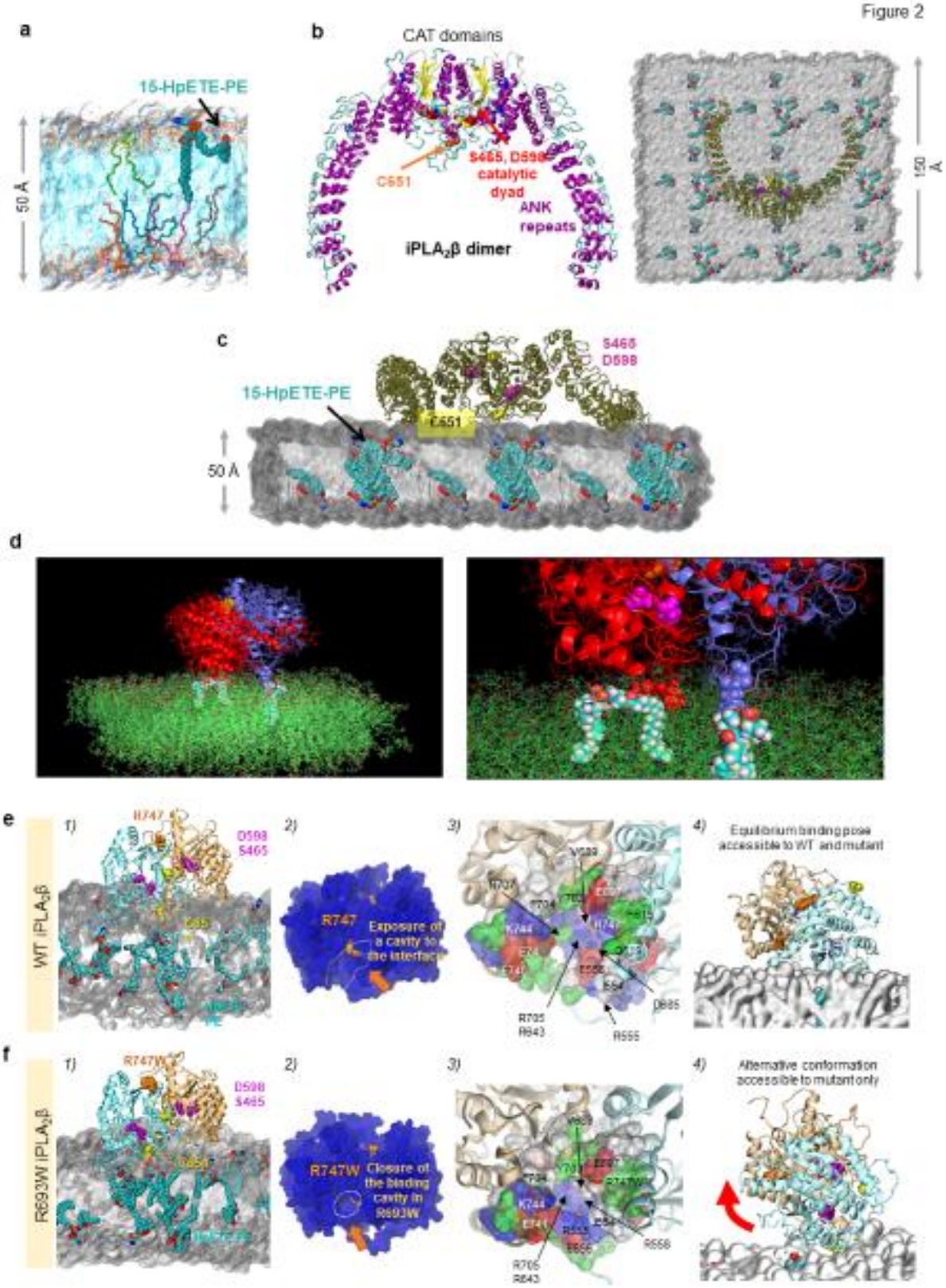
a
15-HpETE-PE
50 Å
b
CAT domains
S465, D588
catalytic
dyad
C551
ANK
repeats
iPLA2β dimer
150 Å
c
S465
D588
15-HpETE-PE
C551
50 Å
d
e
WT iPLA2β
1)
R747
D588
S465
C551
2)
R747
Exposure of
a cavity to
the interface
3)
R705
R843
R555
4)
Equilibrium binding pose
accessible to WT and mutant
f
R693W iPLA2β
1)
R747W
D588
S465
C551
2)
R747W Closure of
the binding
cavity in
R693W
3)
R705
R843
R555
4)
Alternative conformation
accessible to mutant only

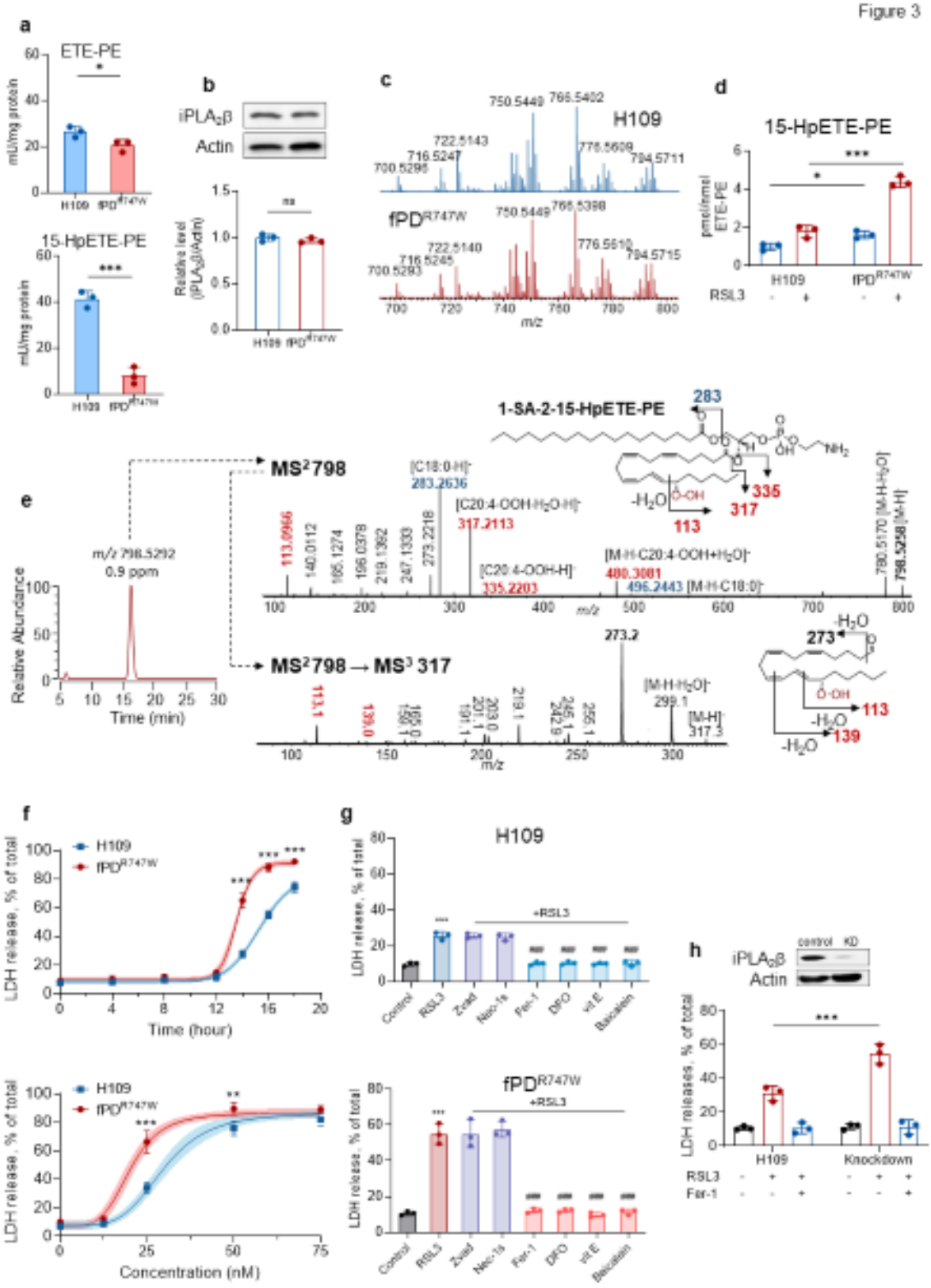
a
ETE-PE
mU/mg protein
H109
fPD R747W
15-HpETE-PE
b
iPLA2β
Actin
Relative level (iPLA2β/Actin)
c
H109
fPD R747W
m/z
d
15-HpETE-PE
pmol/mmol ETE-PE
RSL3
e
m/z 798.5292
0.9 ppm
Relative Abundance
Time (min)
MS2 798
1-SA-2-15-HpETE-PE
MS2 798 → MS3 317
f
H109
fPD R747W
LDH release, % of total
Time (hour)
Concentration (nM)
g
H109
fPD R747W
+RSL3
Control
RSL3
Z-vad
Nec-1s
Fer-1
DFO
vit E
Baicalein
h
iPLA2β
Actin
control
KD
H109
Knockdown
RSL3
Fer-1

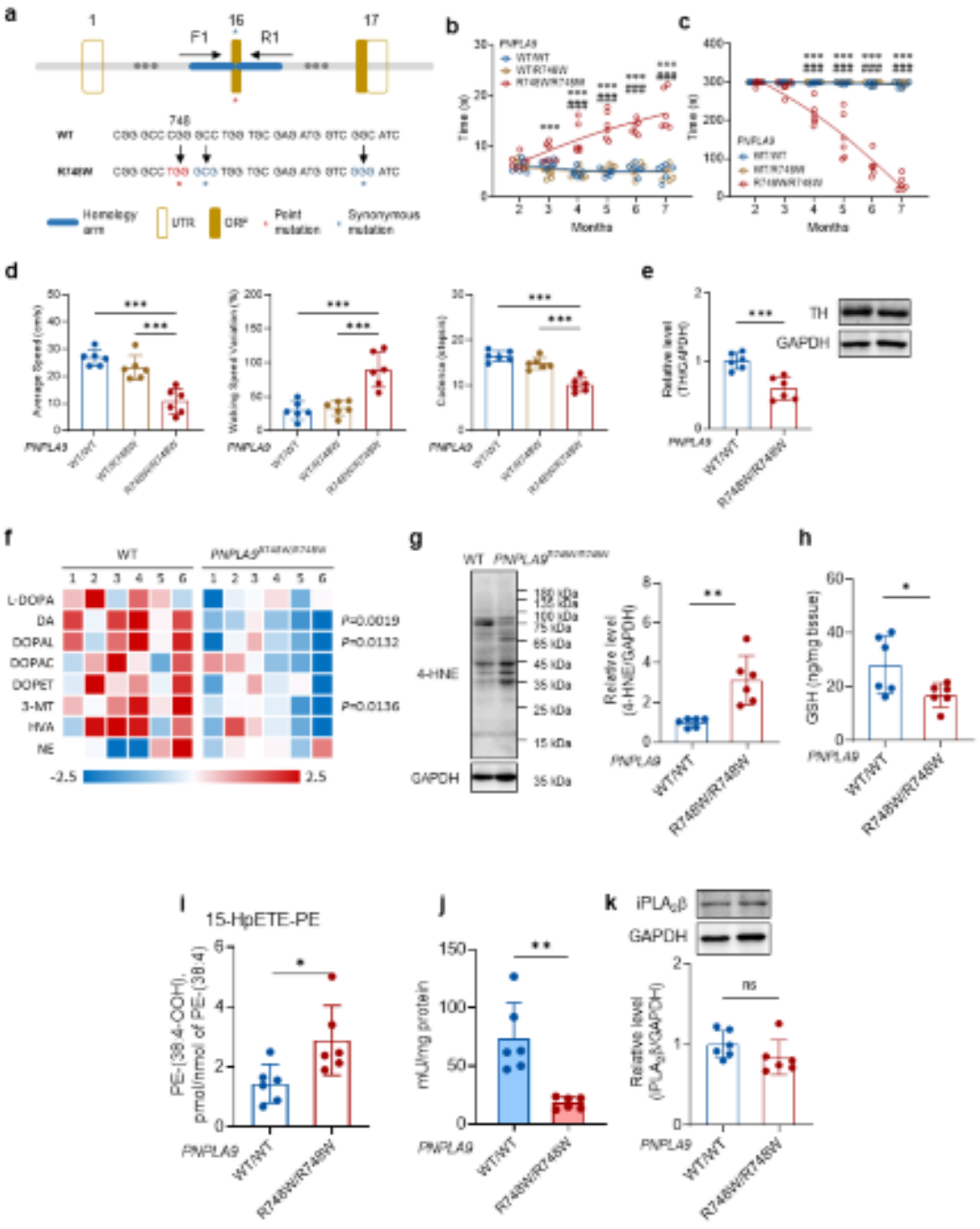
a
1
F1
16
R1
17
748
WT
R748W
Homology arm
UTR
ORF
Point mutation
Synonymous mutation
b
PNPLA9
WT/WT
WT/R748W
R748W/R748W
Time (s)
Months
c
Time (s)
Months
d
Average Speed (cm/s)
Walking Speed Variation (%)
Cadence (steps/s)
e
Relative level (TH/GAPDH)
TH
GAPDH
f
WT
PNPLA9R748W/R748W
L-DOPA
DA
DOPAL
DOPAC
DOPET
3-MT
HVA
NE
P=0.0019
P=0.0132
P=0.0136
-2.5
2.5
g
WT
PNPLA9R748W/R748W
4-HNE
GAPDH
Relative level (4-HNE/GAPDH)
h
GSH (ng/mg tissue)
i
15-HpETE-PE
PE-(38:4-OOH), pmol/nmol of PE-(38:4)
j
mU/mg protein
k
iPLA2β
GAPDH
Relative level (iPLA2β/GAPDH)
ns

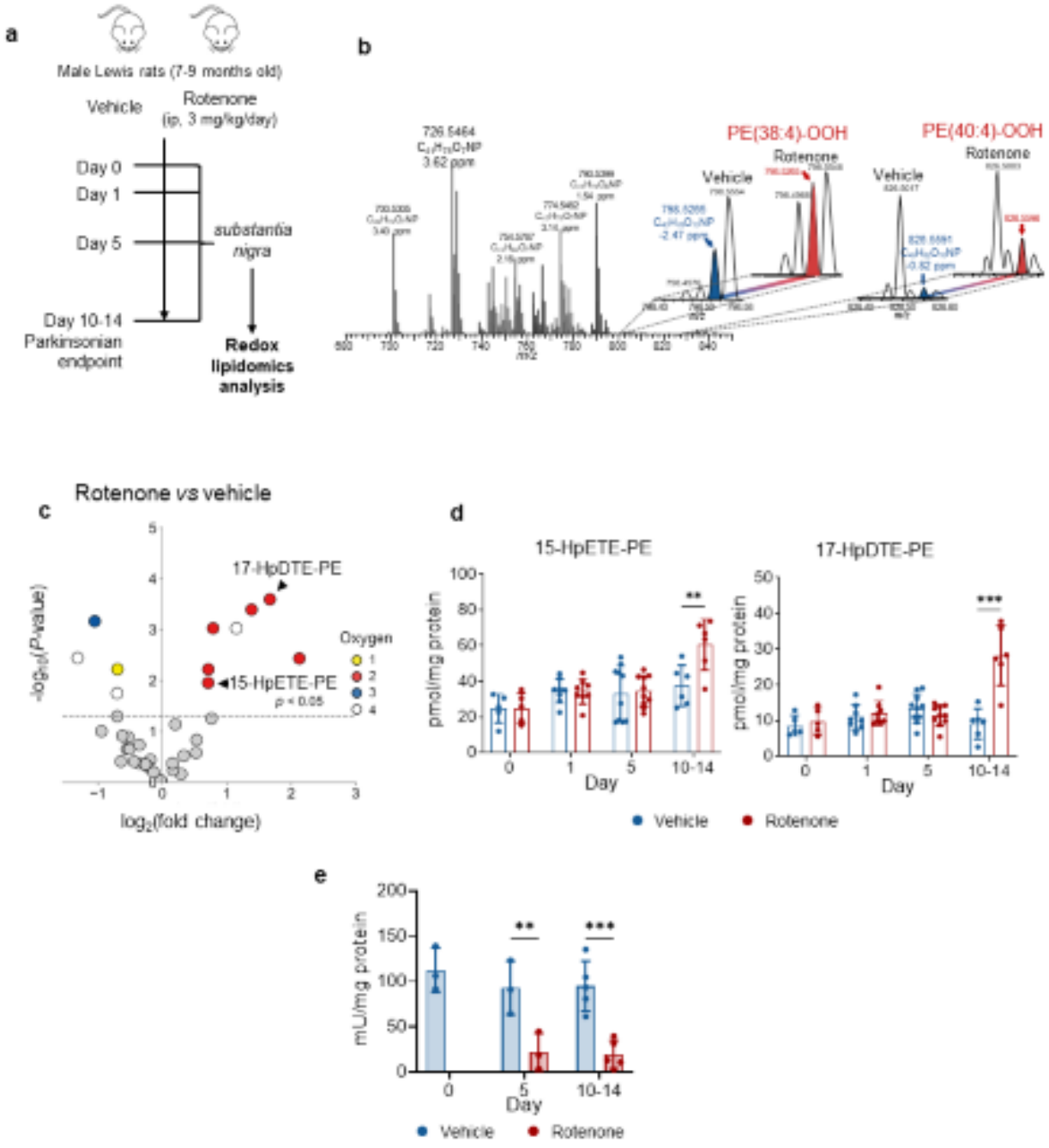
a
Male Lewis rats (7-9 months old)
Vehicle
Rotenone
(ip, 3 mg/kg/day)
Day 0
Day 1
Day 5
Day 10-14
Parkinsonian endpoint
substantia nigra
Redox lipidomics analysis
b
PE(38:4)-OOH
PE(40:4)-OOH
Vehicle
Rotenone
c
Rotenone vs vehicle
17-HpDTE-PE
15-HpETE-PE
p < 0.05
Oxygen
-log10(P-value)
log2(fold change)
d
15-HpETE-PE
17-HpDTE-PE
pmol/mg protein
Day
Vehicle
Rotenone
e
mU/mg protein
Day
Vehicle
Rotenone

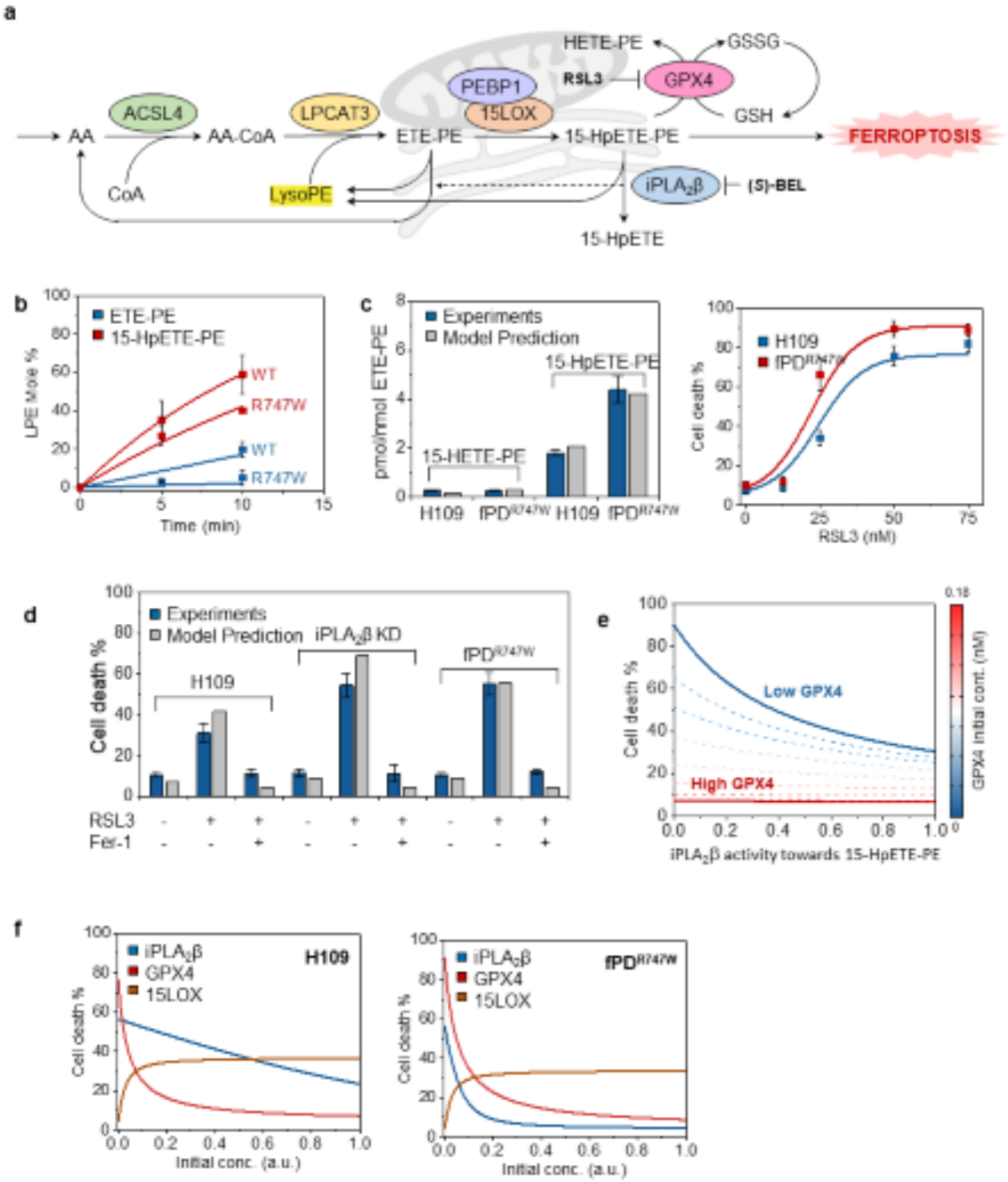
a
HETE-PE
GSSG
RSL3
GPX4
PEBP1
15LOX
GSH
ACSL4
LPCAT3
AA
AA-CoA
ETE-PE
15-HpETE-PE
FERROPTOSIS
CoA
LysoPE
iPLA2β
(S)-BEL
15-HpETE
b
ETE-PE
15-HpETE-PE
LPE Mole %
WT
R747W
WT
R747W
Time (min)
c
Experiments
Model Prediction
15-HpETE-PE
15-HETE-PE
pmol/mol ETE-PE
H109
fPDR747W
H109
fPDR747W
H109
fPDR747W
Cell death %
RSL3 (nM)
d
Experiments
Model Prediction
iPLA2β KD
fPDR747W
H109
Cell death %
RSL3
Fer-1
e
Low GPX4
High GPX4
Cell death %
GPX4 initial cont. (nM)
iPLA2β activity towards 15-HpETE-PE
f
iPLA2β
GPX4
15LOX
H109
Cell death %
Initial conc. (a.u.)
iPLA2β
GPX4
15LOX
fPDR747W
Cell death %
Initial conc. (a.u.)